The Astrophysical Journal, 731:10 (29pp), 2011 April 10 doi:10.1088/0004-637X/731/1/10

RADIAL DISTRIBUTION OF STARS, GAS, AND DUST IN SINGS GALAXIES. III. MODELING THE EVOLUTION OF THE STELLAR COMPONENT IN GALAXY DISKS

J. C. Muñoz-Mateos[1,2], S. Boissier[3], A. Gil de Paz[2], J. Zamorano[2], R. C. Kennicutt, Jr.[4,5], J. Moustakas[6], N. Prantzos[7], and J. Gallego[2]

[1] National Radio Astronomy Observatory, 520 Edgemont Road, Charlottesville, VA 22903-2475, USA; jmunoz@nrao.edu
[2] Departamento de Astrofísica y CC. de la Atmósfera, Universidad Complutense de Madrid, Avda. de la Complutense, s/n, E-28040 Madrid, Spain; gildepaz@gmail.com; jzamorano@fis.ucm.es, j.gallego@fis.ucm.es
[3] Laboratoire d'Astrophysique de Marseille, OAMP, Université Aix-Marseille & CNRS UMR 6110, 38 rue Frédéric Joliot-Curie, 13388 Marseille cedex 13, France; samuel.boissier@oamp.fr
[4] Institute of Astronomy, University of Cambridge, Madingley Road, Cambridge CB3 0HA, UK; robk@ast.cam.ac.uk
[5] Steward Observatory, University of Arizona, Tucson, AZ 85721, USA
[6] Center for Astrophysics and Space Sciences, University of California, San Diego, 9500 Gilman Drive, La Jolla, CA 92093, USA; jmoustakas@ucsd.edu
[7] CNRS, UMR7095, UMPC and Institut d'Astrophysique de Paris, F-75014 Paris, France; prantzos@iap.fr
Received 2010 December 7; accepted 2011 February 1; published 2011 March 17

ABSTRACT

We analyze the evolution of 42 spiral galaxies in the *Spitzer* Infrared Nearby Galaxies Survey. We make use of ultraviolet (UV), optical, and near-infrared radial profiles, corrected for internal extinction using the total-infrared to UV ratio, to probe the emission of stellar populations of different ages as a function of galactocentric distance. We fit these radial profiles with models that describe the chemical and spectro-photometric evolution of spiral disks within a self-consistent framework. These backward evolutionary models successfully reproduce the multi-wavelength profiles of our galaxies, except for the UV profiles of some early-type disks for which the models seem to retain too much gas. From the model fitting we infer the maximum circular velocity of the rotation curve V_C and the dimensionless spin parameter λ. The values of V_C are in good agreement with the velocities measured in H I rotation curves. Even though our sample is not volume limited, the resulting distribution of λ is close to the lognormal function obtained in cosmological *N*-body simulations, peaking at $\lambda \sim 0.03$ regardless of the total halo mass. We do not find any evident trend between λ and Hubble type, besides an increase in the scatter for the latest types. According to the model, galaxies evolve along a roughly constant mass–size relation, increasing their scale lengths as they become more massive. The radial scale length of most disks in our sample seems to have increased at a rate of 0.05–0.06 kpc Gyr^{-1}, although the same cannot be said of a volume-limited sample. In relative terms, the scale length has grown by 20%–25% since $z = 1$ and, unlike the former figure, we argue that this relative growth rate can be indeed representative of a complete galaxy sample.

Key words: galaxies: abundances – galaxies: evolution – galaxies: photometry – galaxies: spiral

Online-only material: figure set

1. INTRODUCTION

Unveiling the details that govern the formation of disk galaxies is paramount for our understanding of the evolution of the universe as a whole. In the currently accepted paradigm of galaxy formation, rotating protogalactic clouds collapse within the gravitational wells of dark matter halos. Gas cools via radiative processes and, if it keeps enough angular momentum, a rotationally supported gaseous disk will eventually form (Fall & Efstathiou 1980; White & Frenk 1991; Mo et al. 1998). Dark matter halos themselves grow from primordial density fluctuations, and they are supposed to merge and evolve according to the Λ Cold Dark Matter model (ΛCDM; Springel et al. 2005; Spergel et al. 2007).

Because gas takes longer to settle onto the disk in the outer parts, given its larger angular momentum and the longer gravitational collapse time, star formation should proceed on longer timescales in the outskirts of disks than in the inner regions. Therefore, a natural consequence of such a scenario is that disk galaxies should be assembled from the inside out (Samland & Gerhard 2003). In particular, the radial scale length of exponential disks is expected to increase with time (Brook et al. 2006; Brooks et al. 2011). In principle, the mass and size evolution of galaxies can be probed with observations at different redshifts (see, e.g., Trujillo et al. 2004, 2006; Barden et al. 2005, and references therein), provided that one can properly deal with cosmological and selection effects.

In a way complementary to this look-back approach, galactic archaeology in the local universe has also proven useful to infer the past evolution of galaxies. Each particular scenario of galactic evolution should have left characteristic imprints in the radial variation of the properties of stars, gas, and dust in present-day galaxies. If galaxies do indeed grow from inside out, stars should be younger on average in the outer parts, leading to radial color gradients such as those we actually observe (de Jong 1996; Bell & de Jong 2000; MacArthur et al. 2004; Taylor et al. 2005; Muñoz-Mateos et al. 2007). Measuring age gradients in disks from color profiles is not straightforward, since the radial decrease in the internal extinction and metallicity also conspire to yield bluer colors at larger radius.

More recently, color–magnitude diagrams of resolved stellar fields in nearby galaxies have also favored an inside-out scenario of galactic growth (Gogarten et al. 2010; Barker et al. 2011). There is also ample observational evidence that chemical abundances decrease with galactocentric distance, both in the Milky Way (MW; Shaver et al. 1983; Smartt & Rolleston 1997) and in external galaxies (Zaritsky et al. 1994; van Zee et al. 1998; Pilyugin et al. 2004; Moustakas & Kennicutt 2006; Moustakas

et al. 2010). Multi-zone chemical evolution models based on the inside-out scenario usually invoke a radially increasing timescale of gas infall to reproduce these metallicity gradients (Matteucci & François 1989; Molla et al. 1996; Prantzos & Boissier 2000; Chiappini et al. 2001; Carigi et al. 2005).

In this paper, the third in a series devoted to the spatial distribution of stars, gas, and dust in nearby galaxies, we will test the predictions of the multi-zone model of Boissier & Prantzos (1999, 2000; BP99 and BP00 hereafter). This model describes the chemical and spectro-photometric evolution of spiral disks in a self-consistent framework, taking into account the radially varying gas infall rate, a physically motivated star formation law, and a full treatment of chemical evolution. The model is first calibrated to reproduce observables of the MW (BP99) and then extended to other disk-like galaxies through scaling laws resulting from the ΛCDM model (BP00). Using only two free parameters, the maximum rotational velocity of the rotation curve V_C and the dimensionless spin parameter λ, the model is able to predict radial profiles of several quantities, including multi-wavelength photometry, metallicity, and gas density among others.

In Muñoz-Mateos et al. (2009a, Paper I hereafter), we derived multi-wavelength profiles from the far-ultraviolet (FUV) to the far-infrared (FIR) for the galaxies in the *Spitzer* Infrared Nearby Galaxies Survey (SINGS; Kennicutt et al. 2003), which comprises 75 objects representative of the typical galaxy population in the Local Universe. In Muñoz-Mateos et al. (2009b, Paper II hereafter) we centered our attention on the radial variation of several physical properties of dust, such as the internal extinction, the dust mass surface density, the abundance of polycyclic aromatic hydrocarbons (PAHs), and the dust-to-gas ratio. In the present paper, we have focused on a subsample of 42 spiral galaxies within the SINGS sample. We have combined the UV, optical, and near-IR profiles measured in Paper I with the extinction profiles obtained in Paper II, in order to recover the intrinsic emission of stars of different ages across the galactic disks. These stellar, extinction-free profiles have been fitted with the models of BP00, thus testing the ability of the models to simultaneously reproduce the multi-band profiles, while at the same time inferring the circular velocities and spin parameters of each object.

The purpose of the present paper is thus twofold: first, we will verify whether the models are able to reproduce the present-day profiles of nearby disks. Second, we will indirectly obtain the values of V_C and λ for each galaxy. The spin parameter is particularly important in cosmological studies. While V_C can be easily determined from rotation curves, λ is not a directly measurable quantity. Previous studies (Syer et al. 1999; Hernandez et al. 2007; Cervantes-Sodi et al. 2008) have shown that λ can be empirically estimated from a combination of observed galactic properties such as the disk scale length, provided that some ΛCDM-based assumptions are made. When applying this methodology to large optical data sets of nearby galaxies, these authors found an excellent agreement between the empirical distribution of λ values and the one obtained in *N*-body simulations of hierarchical clustering. However, optical measurements of disk scale-lengths might be biased by radial variations of the mass-to-light ratio or the internal extinction. The BP00 models incorporate the radial variation of gas infall (inside-out formation) and of the star formation law, thereby accounting for wavelength variations in the disk scale length in a natural way. Moreover, the surface brightness profiles we use to constrain the models are corrected for internal extinction using robust methods (see Paper II). Besides, apart from UV and optical profiles, we incorporate in our analysis near-IR ones, which are less sensitive to mass-to-light variations and dust attenuation. This extra wavelength coverage obviously comes at the expense of using a much more reduced sample than in the aforementioned studies. Therefore, our analysis cannot reach the same levels of statistical completeness, but it should serve nevertheless as a robust foundation for future works.

Features such as bulges, bars, and radial mass flows are not considered in the BP00 models. Accounting for all these effects require *N*-body simulations, which given their complexity are usually limited to a handful of objects. Therefore, despite their somewhat simplified underlying assumptions, models such as the BP00 ones allow simulating large grids of galaxies that cover a wide range of properties, and are therefore better suited for our purposes.

This paper is organized as follows. In Section 2, we provide a brief summary of the inner working of the BP00 models. In Section 3, we describe the main properties of our subsample of SINGS spirals and summarize the procedure used in Paper I to derive the surface brightness profiles. In Section 4, we explain how the multi-wavelength profiles were corrected for the effects of internal extinction. Section 5 deals with the details of the fitting procedure, and in Section 6 we present the main results of our analysis. The main conclusions of this work are summarized in Section 7. Finally, the two-dimensional distribution of χ^2 values resulting from the model fitting is compiled in the Appendix.

2. DESCRIPTION OF THE MODELS

In this section, we broadly outline the main ingredients and underlying assumptions of the chemo-spectrophotometric models used to fit the multi-wavelength profiles of the SINGS galaxies. The reader is referred to BP99 and BP00 for a more in-depth description of the physical details of the models. Briefly, an initial model was first developed and calibrated to reproduce several observed properties of the MW (BP99). This model was then generalized to other spiral disks of different sizes and masses by means of several scaling laws deduced from the ΛCDM scenario of disk formation (BP00).

2.1. The Milky Way Model

The MW disk is modeled as several concentric rings which are progressively built up by accretion of primordial gas from the halo. In the model, these annuli evolve independently from one another, in the sense that no radial mass flows are allowed. Such flows can actually take place in real galaxies as a result, for instance, of the presence of bars (Sellwood & Wilkinson 1993), redistribution of angular momentum due to viscosity (Yoshii & Sommer-Larsen 1989; Ferguson & Clarke 2001), and radial stellar migration (Roškar et al. 2008; Martínez-Serrano et al. 2009; Sánchez-Blázquez et al. 2009). In particular, stellar migration has been proposed as a likely mechanism to explain the observed U-shaped color profiles in galaxies (Azzollini et al. 2008a; Bakos et al. 2008). Moreover, gas outflows are not included in the models, while observations suggest that they play a role in the chemical evolution of low-mass galaxies (Garnett 2002). Nevertheless, this is likely not a concern in our analysis, since most of our disks are large and massive enough. Finally, the model does not include the bulge nor does it differentiate between the thin and thick disk. Implementing all these phenomena in an analytic way is not straightforward,

and it would introduce many additional free parameters whose values might be difficult to constrain. Despite the simplifying assumption of independently evolving rings, the model is still successful at reproducing the radial structure of the MW.

The star formation rate (SFR) surface density at each radius r and time t, $\Sigma_{\rm SFR}(t, r)$, depends on the local gas density $\Sigma_{\rm g}(t, r)$ following a Schmidt law modulated by a dynamical term:

$$\Sigma_{\rm SFR}(t, r) = \alpha \Sigma_{\rm g}(t, r)^n V(r) r^{-1}. \quad (1)$$

Here $V(r)$ is the rotational velocity at radius r. The term $V(r)r^{-1}$ is intended to mimic the conversion of gas into stars by the periodic passage of spiral density waves (Wyse & Silk 1989); it can be also seen as the inverse of a dynamical timescale. Originally, α was fixed in order to reproduce the local gas fraction in the solar neighborhood at $T = 13.5$ Gyr, and $n = 1.5$ was chosen to reproduce radial trends. Later on, in Boissier et al. (2003) the star formation law was empirically determined using a sample of nearby galaxies. Here, we adopt the values of $\alpha = 0.00263$[8] and $n = 1.48$ found in that work. Note that these values are very close to the ones originally adopted in BP99 and BP00 ($\alpha = 0.00364$ and $n = 1.5$).

The gas infall rate $f(r, t)$ decreases exponentially with time:

$$f(t, r) = A(r) e^{-t/\tau(r)}. \quad (2)$$

The timescale of gas accretion $\tau(r)$ is assumed to increase with radius, from 1 Gyr at $r = 1$ kpc to 15 Gyr at $r = 17$ kpc. This allows the reproduction of the inside-out formation of disks, since gas settles onto the disk on longer timescales in the outer regions as they have large angular momentum. At $r = 8$ kpc τ is set equal to 7 Gyr to reproduce the metallicity distribution of G-dwarf stars in the solar neighborhood. The normalizing factor $A(r)$ can be deduced by integrating the infall rate until $T = 13.5$ Gyr, and then matching the result to the current stellar mass profile of the disk:

$$\int_0^T f(t, r) dt = \Sigma_{\text{solar neigh.}} e^{-(r-8\ \text{kpc})/R_{\rm dG}} = \Sigma_{\rm 0G} e^{-r/R_{\rm dG}}. \quad (3)$$

The subscript "G" refers to the parameters of our Galaxy. According to observations of the MW, the radial scale length is fixed to $R_{\rm dG} = 2.6$ kpc, and the central mass density (extrapolated from the one in the solar neighborhood) is set to $\Sigma_{\rm 0G} = 1150\ M_\odot\ {\rm pc}^{-2}$ (see BP99 for references).

The distribution of stars for a given SFR follows a user-specified initial mass function (IMF). Even though we are explicitly assuming the existence of a universal IMF, this might not necessarily be the case (see Bastian et al. 2010 for a review on the subject). Therefore, in this work we will compare the results obtained with the IMFs of Kroupa et al. (1993; K93 hereafter) and Kroupa (2001; K01 hereafter). The K93 IMF was used in the original models, but here we are also interested in analyzing the results yielded by a more recent version of the IMF. The optical and near-IR fluxes, as well as the gas quantities, change by less than 20% between these two IMFs, which justifies not to totally recalibrate the model. It is the UV fluxes and metallicities that vary significantly, given the different content in high-mass stars of both IMFs (see Section 6.2.3). Of course, there exist several other parameterizations of the IMF which are widely used in extragalactic studies, but the comparison between the K93 and K01 IMFs presented here should suffice for the purpose of showing the impact of varying the relative amount of high- and low-mass stars.

Stars of different masses enrich the ISM with varying amounts of different elements; in this regard, the model does not assume the instantaneous recycling approximation (Tinsley 1980), according to which stars more massive than $1\ M_\odot$ die instantly, whereas less massive ones live forever. On the contrary, the model takes into account the finite lifetimes of stars of different masses when computing the chemical evolution within each ring. Moreover, the properties of each new generation of stars (lifetimes, stellar yields, evolutionary tracks, and spectra) depend on the local metallicity at the corresponding radius and time of formation (see BP99). The spectrum of a given ring at time t can be then computed as the sum (both in time and mass) of the individual spectra of previously formed stars which are still alive at time t.

With the assumptions outlined above, BP99 showed that their MW model is able to reproduce not only observables in the solar neighborhood, but also radially dependent ones, such as profiles of gas surface density, gas-phase oxygen abundance, SFR, and supernova rates, as well as luminosity profiles at different bands.

2.2. Extension to Other Disk-like Galaxies

The previous model for the MW was generalized to other disks in BP00 by making use of the scaling laws derived by Mo et al. (1998) within the ΛCDM scenario. In this theoretical framework, galaxy formation is usually split into two different processes: the growth of non-baryonic dark matter halos and the assembly of baryonic structures within them. Gravitational instabilities amplify the primordial density fluctuations, yielding dark matter clumps that merge and interact with each other, acquiring angular torques during the process. Meanwhile, baryonic gas cools and condenses within these halos, leading to self-gravitating structures that are able to form stars, thus eventually giving rise to present-day galaxies.

The models of BP00 build on the mathematical formalism of Mo et al. (1998), which establishes that under certain assumptions the scaling properties of disks depend only on two parameters: the maximum circular velocity of the rotation curve $V_{\rm C}$ and the dimensionless spin parameter λ:

$$V_{\rm C} = [10GH(z)M]^{1/3} \quad (4)$$

$$\lambda = J|E|^{1/2} G^{-1} M^{-5/2}. \quad (5)$$

In the equations above, M, J, and E are the total mass, angular momentum, and energy of the halo, G is the gravitational constant, and $H(z)$ is the Hubble parameter at the redshift z of halo formation. In order to express the properties of disks in terms of $V_{\rm C}$ and λ alone, the following assumptions need to be made.

1. The masses of disks $M_{\rm d}$ are just a few percent of those of their corresponding halos. The precise value of this ratio is unclear, but it must conform to the baryonic fraction of the universe and the efficiency of disk formation. Following Mo et al. (1998), the BP00 models assume $M_{\rm d} = 0.05M$ for all disks.
2. The specific angular momenta of the disk and halo are equal (i.e., $J_{\rm d}/M_{\rm d} = J/M$). While this commonly used assumption is not strictly supported by numerical simulations, it is apparently required to produce disk sizes that match observations.

[8] The units of α are such that $\Sigma_{\rm SFR}(r)$ is measured in $M_\odot\ {\rm pc}^{-2}\ {\rm Gyr}^{-1}$, $\Sigma_{\rm gas}(r)$ in $M_\odot\ {\rm pc}^{-2}$, r in kpc, and $V(r)$ in km s^{-1}. See also Figure 17.

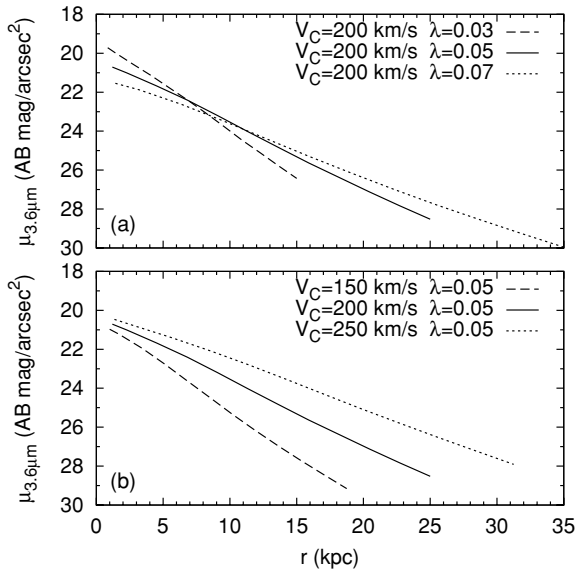

Figure 1. Sample surface brightness profiles generated by the model at 3.6 μm, showing the effect of varying (a) the spin parameter and (b) the circular velocity.

3. Variations in the formation time of the disks are ignored. It is now believed that the thin component of disks is assembled at $z \sim 1$ (Brook et al. 2006), and its evolution dominates the inside-out growth of spirals until $z = 0$ (Chiappini et al. 1997). However, disks might contain stellar populations that formed much earlier. The concept of "formation time" is thus somehow ill-defined, and the BP00 models simply assume that all disks started forming stars at the same time, having today a fixed age of 13.5 Gyr.

Under these assumptions, BP00 showed that the scale length R_d and central mass density Σ_0 of a given disk can be derived from those of the MW by means of their relative spins and circular velocities:

$$\frac{R_d}{R_{dG}} = \frac{\lambda}{\lambda_G}\frac{V_C}{V_{CG}} \quad (6)$$

$$\frac{\Sigma_0}{\Sigma_{0G}} = \left(\frac{\lambda}{\lambda_G}\right)^{-2}\frac{V_C}{V_{CG}}. \quad (7)$$

For the case of the MW, the BP00 models assume that $V_{CG} = 220$ km s^{-1} and $\lambda_G = 0.03$. Although both V_C and λ affect the final scale length of a disk, they do it in different ways, as can be seen in Figure 1. Larger values of V_C yield more extended and massive disks, while modifying λ alters the scale length alone.

Note that when calibrating our model on the MW, we are implicitly assuming some sort of homology between the evolution of the galaxies we study and the MW. This homology is observationally motivated by the fact that several properties of galaxies such as metallicity gradients (Garnett et al. 1997; Henry & Worthey 1999) or rotation curves (Salucci & Persic 1997) become "universal" once normalized by the optical size. Nevertheless, homology constitutes a simplifying assumption that may be partly responsible of some of the discrepancies that we will show later.

The scaling laws described above affect the way in which the SFR and the gas infall timescale depend on galactocentric distance. The final rotation curve of a given simulated galaxy is computed as the sum of the contributions of the halo and the disk. The resulting function $V(r)$ is then used through Equation (1) to determine the radial variation of the SFR. The timescale for the gas infall is parameterized as a function of both the local mass surface density and the total galaxy's mass, in the sense that a deeper gravitational well leads to a more rapid infall of gas onto the disk (see Equation (21) and Figure 3 in BP00).

3. THE DATA

From the original 75 objects of the SINGS sample we first exclude all ellipticals, lenticulars, and dwarf irregulars, leaving only those galaxies with morphological types $1 \leqslant T \leqslant 9$. From the remaining list of galaxies we also exclude the following objects.

1. NGC 2798, an Sa galaxy with a severely distorted morphology due to its interaction with the neighbor galaxy NGC 2799.
2. NGC 3190 and NGC 4594 (The Sombrero Galaxy). These Sa galaxies are seen almost edge-on, with dense dust lanes heavily obscuring part of their disks. Besides, their prominent bulges modify the ellipticity of the isophotes used to measure their surface brightness profiles, which may not be representative of their disk components alone.
3. NGC 4631, an edge-on Sd galaxy for which our elliptical isophotes probably mix light emitted at very different galactocentric distances.
4. NGC 5474, an Scd galaxy with a disturbed morphology, probably due to a tidal interaction with M101. In the optical and near-IR, its main disk is significantly shifted southward with respect to the bulge.

Even though NGC 5194 (M51a) is clearly interacting with NGC 5195 (M51b), we do not exclude it from our analysis, since it still retains its axial symmetry. After applying these criteria we are left with 42 disk-like galaxies, whose main properties are summarized in Table 1.

We refer the reader to Paper I for a detailed description of the imaging data set employed here. UV images were taken with the *GALEX* space telescope (Martin et al. 2005) in the FUV and NUV bands, and belong to the sample compiled in the *GALEX* Atlas of Nearby Galaxies (Gil de Paz et al. 2007). We employed two sets of optical images. On one hand, we relied on *ugriz* images from the Sloan Digital Sky Survey DR6 (SDSS; York et al. 2000; Adelman-McCarthy et al. 2008) when available. For objects without SDSS imaging, we used the original SINGS optical images (Dale et al. 2007), taken with the Kitt Peak National Observatory (KPNO) 2.1 m telescope and the Cerro Tololo Inter-American Observatory (CTIO) 1.5 m telescope. Some of these *BVRI* optical images were affected by zero-point offsets that were corrected in Paper I. Note that this recalibration procedure adds an extra component to the photometric uncertainty of the *BVRI* fluxes that is not present in the SDSS ones.

Near-IR images in the J, H, and K_S bands were compiled from the 2MASS Large Galaxy Atlas (Jarrett et al. 2003). Finally, we also used images at 3.6 μm and 4.5 μm, taken with the Infrared Array Camera (IRAC; Fazio et al. 2004) onboard *Spitzer* (Werner et al. 2004). Since we are interested in tracing the stellar emission, we did not consider the other two IRAC bands at 5.8 μm and 8.0 μm, which contain significant emission from hot dust and PAHs. However, we did use those bands, together with the FIR bands at 24, 70, and 160 μm from the Multi-band Imaging Photometer (MIPS; Rieke et al.

Table 1
Sample

Object Name	R.A.$_{2000}$ (h m s)	Decl.$_{2000}$ (d:m:s)	$2a$ (arcmin)	$2b$ (arcmin)	P.A. (deg)	$E(B-V)$ (mag)	Distance (Mpc)	T Type	Morphological Type	r_{in} (arcsec)	r_{out} (arcsec)
(1)	(2)	(3)	(4)	(5)	(6)	(7)	(8)	(9)	(10)	(11)	(12)
NGC 0024	00 09 56.5	−24 57 47.3	5.8	1.3	46	0.020	8.2	5	SA(s)	48	...
NGC 0337	00 59 50.1	−07 34 40.7	2.9	1.8	310	0.112	25	7	SB(s)d	30	...
NGC 0628	01 36 41.8	15 47 00.5	10.5	9.5	25	0.070	11	5	SA(s)c	54	...
NGC 0925	02 27 16.9	33 34 45.0	10.5	5.9	282	0.076	9.3	7	SAB(s)d	66	...
NGC 1097	02 46 19.1	−30 16 29.7	9.3	6.3	310	0.027	15	3	SB(s)b	54	...
NGC 1512	04 03 54.3	−43 20 55.9	8.9	5.6	90	0.011	10	1	SB(r)a	48	300
NGC 1566	04 20 00.4	−54 56 16.1	8.3	6.6	60	0.009	17	4	SAB(s)bc	30	...
NGC 2403	07 36 51.4	65 36 09.2	21.9	12.3	307	0.040	3.2	6	SAB(s)cd	24	...
NGC 2841	09 22 02.6	50 58 35.5	8.1	3.5	327	0.016	14	3	SA(r)b	90	...
NGC 2976	09 47 15.5	67 54 59.0	5.9	2.7	323	0.069	3.6	5	SAc pec	...	...
NGC 3049	09 54 49.7	09 16 17.9	2.2	1.4	25	0.038	22	2	SB(rs)ab	18	...
NGC 3031	09 55 33.2	69 03 55.1	26.9	14.1	337	0.080	3.6	2	SA(s)ab	204	900
NGC 3184	10 18 17.0	41 25 28.0	7.4	6.9	135	0.017	8.6	6	SAB(rs)cd	48	...
NGC 3198	10 19 54.9	45 32 59.0	8.5	3.3	35	0.012	17	5	SB(rs)c	48	...
IC 2574	10 28 23.5	68 24 43.7	13.2	5.4	50	0.036	4.0	9	SAB(s)m	...	...
NGC 3351	10 43 57.7	11 42 13.0	7.4	5.0	13	0.028	12	3	SB(r)b	48	...
NGC 3521	11 05 48.6	−00 02 09.1	11.0	5.1	343	0.058	9.0	4	SAB(rs)bc	48	...
NGC 3621	11 18 16.5	−32 48 50.6	12.3	7.1	339	0.080	8.3	7	SA(s)d	48	230
NGC 3627	11 20 15.0	12 59 29.6	9.1	4.2	353	0.032	9.1	3	SAB(s)b	48	...
NGC 3938	11 52 49.4	44 07 14.6	5.4	4.9	15	0.021	12	5	SA(s)c	48	...
NGC 4236	12 16 42.1	69 27 45.3	21.9	7.2	342	0.015	4.5	8	SB(s)dm	...	...
NGC 4254	12 18 49.6	14 24 59.4	5.4	4.7	35	0.039	17	5	SA(s)c	48	...
NGC 4321	12 22 54.9	15 49 20.6	7.4	6.3	30	0.026	18	4	SAB(s)bc	60	...
NGC 4450	12 28 29.6	17 05 05.8	5.2	3.9	355	0.028	17	2	SA(s)ab	48	...
NGC 4536	12 34 27.1	02 11 16.4	7.6	3.2	310	0.018	15	4	SAB(rs)bc	48	...
NGC 4559	12 35 57.7	27 57 35.1	10.7	4.4	330	0.018	17	6	SAB(rs)cd	48	...
NGC 4569	12 36 49.8	13 09 46.3	9.5	4.4	23	0.046	17	2	SAB(rs)ab	48	...
NGC 4579	12 37 43.6	11 49 05.1	5.9	4.7	275	0.041	17	3	SAB(rs)b	48	...
NGC 4625	12 41 52.7	41 16 25.4	2.2	1.9	330	0.018	9.5	9	SAB(rs)m pec	...	50
NGC 4725	12 50 26.6	25 30 02.7	10.7	7.6	35	0.012	17	2	SAB(r)ab pec	96	...
NGC 4736	12 50 53.1	41 07 13.6	11.2	9.1	285	0.018	5.2	2	(R)SA(r)ab	75	230
NGC 4826 ‡	12 56 43.8	21 40 51.9	10.0	5.4	295	0.041	7.5	2	(R)SA(rs)ab	96	...
NGC 5033	13 13 27.5	36 35 38.0	10.7	5.0	170	0.011	13	5	SA(s)c	96	...
NGC 5055	13 15 49.3	42 01 45.4	12.6	7.2	285	0.018	8.2	4	SA(rs)bc	96	...
NGC 5194 †	13 29 52.7	47 11 42.6	11.2	9.0	0	0.035	8.4	4	SA(s)bc pec	48	400
TOL 89	14 01 21.6	−33 03 49.6	2.8	1.7	352	0.066	16	8.1	(R')SB(s)dm pec	...	...
NGC 5713	14 40 11.5	−00 17 21.2	2.8	2.5	10	0.039	27	4	SAB(rs)bc pec	...	...
IC 4710	18 28 38.0	−66 58 56.0	3.6	2.8	5	0.089	8.5	9	SB(s)m	...	...
NGC 6946	20 34 52.3	60 09 14.2	11.5	9.8	75	0.342	5.5	6	SAB(rs)cd	48	400
NGC 7331	22 37 04.1	34 24 56.3	10.5	3.7	351	0.091	15	3	SA(s)b	96	...
NGC 7552	23 16 10.8	−42 35 05.4	3.4	2.7	1	0.014	22	2	(R')SB(s)ab	24	...
NGC 7793 ‡	23 57 49.8	−32 35 27.7	9.3	6.3	278	0.019	3.9	7	SA(s)d	48	...

Notes. Main properties of the sample. (1) Galaxy name; (2, 3) R.A.(J2000) and decl.(J2000) of the galaxy center; (4, 5) apparent major and minor isophotal diameters at $\mu_B = 25$ mag arcsec^{-2} from the RC3 catalog; (6) position angle from RC3. † The P.A. and axis ratio of NGC 5194 adopted here differ from those in RC3, which are affected by the presence of NGC 5195. (7) Galactic color excess from Schlegel et al. (1998); (8) distance to the galaxy, rounded to the nearest Mpc when larger than 10 Mpc, taken from Gil de Paz et al. (2007) and Kennicutt et al. (2003). ‡ The distances to NGC 4826 and NGC 7793 have been updated with respect to those used in Papers I and II. (9) Morphological type T as given in RC3 catalog; (10) full description of the morphological type from RC3. (11, 12) Inner and outer limits along the semimajor axis used to restrict the fitting procedure.

2004) to compute the radial variation of internal extinction from the TIR/FUV and TIR/NUV ratios (see Paper II and Section 4).

Technical details on how the radial profiles were obtained are also given in Paper I. Briefly, we used the IRAF[9] task ELLIPSE to measure the mean surface brightness along concentric elliptical isophotes, using the same sets of ellipses at all bands for each galaxy. The ellipticity and position angle were kept fixed and equal to those of the $\mu_B = 25$ mag arcsec^{-2} isophote from the RC3 catalog (de Vaucouleurs et al. 1991), or from the NASA Extragalactic Database (NED) when these parameters were not included in RC3. They are quoted in Table 1 together with the central coordinates of the ellipses, which were also kept fixed. We used radial increments of 6″ along the semimajor axis (similar to the FWHM of the *GALEX* PSF) up to a final radius at least 1.5 times the diameter at $\mu_B = 25$ mag arcsec^{-2} (D25). This upper limit was increased when significant emission was seen beyond that radius (especially in the UV bands). The uncertainty of the mean surface brightness at each radius comprises the Poisson noise in the source flux and the error in the sky level, the

[9] IRAF is distributed by the National Optical Astronomy Observatory, which is operated by the Association of Universities for Research in Astronomy, Inc., under cooperative agreement with the National Science Foundation.

latter including both local and large-scale background variations (see Paper I).

4. INTERNAL EXTINCTION CORRECTION

Prior to fitting the multi-wavelength profiles, we must first correct them for the radial variation of the internal attenuation.[10] In Paper II, we computed internal attenuation profiles in the FUV and NUV bands independently from the TIR/FUV and TIR/NUV ratios, respectively. We followed the prescriptions of Cortese et al. (2008), which take into account the varying extra dust heating due to evolved stellar populations. After $A_{\rm FUV}$ and $A_{\rm NUV}$ have been obtained, the attenuation at other wavelengths can be derived after assuming a given extinction law and a geometry for the distribution of stars and dust. Here we follow the prescriptions of Boselli et al. (2003) and adopt a sandwich model, where a thin layer of dust is embedded in a thicker layer of stars:

$$A_i(\lambda) = -2.5\log\left(\left[\frac{1-\zeta(\lambda)}{2}\right](1+e^{-\tau(\lambda)\sec(i)}) + \left[\frac{\zeta(\lambda)}{\tau(\lambda)\sec(i)}\right](1-e^{-\tau(\lambda)\sec(i)})\right). \quad (8)$$

Here $\tau(\lambda)$ is the face-on optical depth and i is the inclination angle. Note that we need not to care about them separately as $\tau(\lambda)\sec(i)$ is a joint quantity. The variable $\zeta(\lambda)$ denotes the ratio between the thickness of the dust and star layers. Young stars, which dominate the emission in the UV range, are likely immersed in a thin dust layer. More evolved ones, which emit most of their light predominantly in the optical and near-IR bands, migrate with time out of the galactic plane, and are thus assumed to lie within a thicker layer, partly above and below the thin dust layer. Therefore, Boselli et al. (2003) parameterize the dust-to-stars scale-height ratio as a decreasing function of λ:

$$\zeta(\lambda) = 1.0867\text{–}5.501 \times 10^{-5}\lambda, \quad (9)$$

where λ is measured in Å. Equation (9) was obtained from the λ-dependent scale-height ratios given in Boselli & Gavazzi (1994), by averaging the optically thin and optically thick cases. In the UV ($\lambda \simeq 2000$ Å), this ratio is $\zeta = 1$, so Equation (8) reduces to a slab model and can be numerically inverted:

$$\tau(\mathrm{UV})\sec(i) = 0.0259 + 1.2002 \times A_i(\mathrm{UV}) + 1.5543 \times A_i(\mathrm{UV})^2 - 0.7409 \times A_i(\mathrm{UV})^3 + 0.2246 \times A_i(\mathrm{UV})^4. \quad (10)$$

Once the optical depth in the UV is known, the corresponding value at any other wavelength is given by a particular extinction law $k(\lambda)$:

$$\tau(\lambda) = \tau(\mathrm{UV}) \times k(\lambda)/k(\mathrm{UV}), \quad (11)$$

which plugged into Equation (8) gives us the attenuation at the desired band.

The conversion between the TIR/FUV and TIR/NUV ratios into $A_{\rm FUV}$ and $A_{\rm NUV}$, respectively, is rather insensitive to the adopted extinction law (Cortese et al. 2008). Nevertheless, to compute the extinction at other wavelengths we must not only choose a particular extinction law, but also decide whether to determine $A(\lambda)$ by extrapolating from $A_{\rm FUV}$ or $A_{\rm NUV}$ in the equations above. Here we use the MW extinction law of Li & Draine (2001), assuming $R_V = 3.1$. Other extinction curves are possible, but most of them agree pretty well from the near-IR to the NUV bands (Gordon et al. 2003). It is beyond the 2175 Å bump that large differences arise. Therefore, in order to minimize the impact of our particular choice of extinction law, we use the NUV band rather than the FUV one in Equations (10) and (11).

5. FITTING PROCEDURE

In order to find the model that best fits the observed multi-wavelength profiles for each galaxy, a χ^2 minimization procedure was followed. We generated a grid of models with velocities ranging between 130 and 250 km s^{-1} in steps of 10 km s^{-1}, plus extra values of 40, 80, 290, and 360 km s^{-1}. As for the spin parameter, we sampled the interval $0.02 \leqslant \lambda \leqslant 0.09$ in steps of 0.01; we also added $\lambda = 0.10, 0.15$, and 0.20 to our grid in order to account for possible low surface brightness galaxies (LSBs).

Taking this set of 187 pre-computed models as our starting point, we used a two-dimensional interpolation algorithm to generate a finer grid of models with steps of 0.001 in λ and 1 km s^{-1} in $V_{\rm C}$. We verified that any given property of a model galaxy at a certain radius varies smoothly enough with λ and $V_{\rm C}$, so that the corresponding value for a model with an intermediate spin and velocity can be indeed approximated by means of a two-dimensional interpolation.

The total χ^2 of each model was computed by summing over data points at all bands and galactocentric distances. By visually inspecting the multi-wavelength profiles, we excluded from the fit those radial ranges in which the overall emission is dominated by the bulge. In those galaxies with sharp outer truncations or anti-truncations—which the BP00 models cannot reproduce by construction—the outermost regions were excluded as well. This affects NGC 1512, NGC 3621, NGC 4625, and NGC 4736, so for these objects the results of the fitting only concern the bright inner disk.[11] The radial range used for the fit in each galaxy is quoted in Table 1.

The resulting distribution of χ^2 values are shown in the Appendix. If they are to be used to derive confidence intervals for the fitted parameters, rather than just to find the best-fitting values, then a proper determination of the uncertainties of each data point and of the models is mandatory. In principle, the χ^2 method assumes that any deviation of the observed values with respect to the model predictions is entirely due to measurement errors. If these errors are properly accounted for when computing χ^2, then the confidence intervals for the fitted parameters are defined by all models with $\chi^2 < \chi^2_{\rm min} + \Delta\chi^2$, where $\Delta\chi^2$ depends on the confidence level and the number of parameters that are being estimated simultaneously (see, e.g., Avni 1976; Press et al. 1992).

However, we cannot strictly follow this approach in our case, because the models do not reproduce the small-scale structures

[10] Note that when interacting with dust grains, photons can be absorbed, scattered out of the line of sight, and scattered back into it. The term "extinction" refers to the first two processes, while "attenuation" encompasses all of them. When talking about external galaxies the term "attenuation" is preferred, since it takes into account the complex radiative transfer processes resulting from the relative geometry of stars and dust. Nevertheless, with this caveat in mind we will use both terms interchangeably throughout this paper.

[11] More galaxies in the sample exhibit multi-sloped profiles, but their breaks are considerably smeared out in the optical and especially in the near-IR. Indeed, excluding the outer disks does not perceptively change the output of the fit in those cases. For NGC 3031, NGC 5194, and NGC 6946, though, we did exclude the very outermost parts of the profiles due to contamination from noisy background structures.

of real disks. In an attempt to overcome this problem, we first run our fitting code assuming that the total uncertainty for each data point is the quadratic sum of the photometric and zero-point errors, plus an extra uncertainty of 10%. This additional term serves as an initial guess for the intrinsic error of the model, and also avoids giving excessive weight to any particular band and/or data-point. The typical reduced χ^2 at this stage is of the order of ∼5. We then compute the relative rms of the best-fitting model with respect to the galaxy's profiles, both as a function of radius and wavelength. In this way, we can estimate how well we can expect the model to fit that particular galaxy at each band. These "error profiles" are then fed to the code in a second run, in place of the initial uncertainties. The new reduced χ^2 values are now close to 1, by construction. However, the purpose of this two-stage fitting process is not to artificially bring the reduced χ^2 closer to unity, but to properly take into account deviations due to small-scale features that the models, by construction, are not able to reproduce.

Even after following this process, we found that the technique of adding a constant $\Delta\chi^2$ offset to the total (i.e., not reduced) χ^2 still yielded unrealistically small confidence intervals for V_C and λ. A visual inspection confirmed that indeed many models outside these confidence regions were still in very good agreement with the observed profiles. Thus, we finally opted for defining the boundaries of the confidence intervals with those models whose total χ^2 is twice the minimum one. Therefore, although the resulting errors in λ and V_C cover the range of models that visually agree with the galaxy's profiles, they are indicative and should not be interpreted in a strict statistical way (see also Boselli et al. 2006 in this regard).

As an example, in Figure 2 we show the resulting fit for the Sc spiral NGC 3198 using the K01 IMF (see the online edition of the journal for similar plots for the remaining galaxies). The gray data points show the observed profiles, corrected only for MW extinction, while the black ones are also corrected for internal extinction. Both profiles have been deprojected to their face-on values by means of the galaxy's morphological axis ratio.[12] The fit is applied to the profiles corrected for internal extinction, and only to those points beyond the red dashed line, which separates the bulge- and disk-dominated regions of the profiles. In the few cases where we had to exclude the outer regions (due to strong up-bendings, for instance), the outer limit is marked with a blue dashed line. The best-fitting model is shown with a red line, and the band with a lighter shade of red contains all models with $\chi^2 \leqslant 2\chi^2_{\rm min}$.

However, the fit is not always equally good at all wavelengths. In Figure 3, we show the best-fitting model for the Sb galaxy NGC 2841. Even though the quality of the fit is excellent all the way from 4.5 μm to the *u* band, the model overpredicts the luminosity of the galaxy in the *GALEX* bands. This tends to happen mostly in early-type spirals, as will be discussed in Section 6.2.3.

6. RESULTS

6.1. Global Properties

The results of the fitting procedure are quoted in Table 2. Prior to going further in our analysis, we will briefly describe the statistical distribution of the model parameters λ and V_C. As mentioned before, for each galaxy we have run our fitting code using both the K93 and K01 IMFs. Given their different content in high-mass stars at a fixed total mass, the resulting profiles differ in the UV bands, but agree in the optical and near-IR ones. The effects of choosing one IMF or another will be discussed in detail in Section 6.2.3, but for now it will suffice to say that neither λ nor V_C are significantly affected by our particular choice of IMF. Therefore, hereafter we use the K93 IMF as our default choice, unless otherwise mentioned.

6.1.1. Statistical Distribution of the Model Parameters

In Figure 4, we show the resulting histograms of both fitting parameters. It can be seen that most galaxies exhibit values of λ and V_C similar to those of the MW. In particular, the distribution of rotational velocities peaks at 200–220 km s^{-1}. It should be noted, however, that neither the SINGS sample nor the smaller subsample of disks considered here is complete. The well-known Schechter (1976) function can be used to fit not only the mass and luminosity functions of nearby galaxies (Bell et al. 2003), but also their circular velocity distribution (Gonzalez et al. 2000; Boissier et al. 2010). In this sense, low-mass slow-rotating disks are known to outnumber more massive and faster-rotating ones. Therefore, the velocity distribution shown in Figure 4 obviously underestimates the number of low-velocity galaxies that would be found in a volume-limited sample.

Regarding the spin parameter, most disks in our sample have $\lambda \sim 0.03$, the same spin we have adopted for the MW. Had we chosen a different MW spin, the resulting distribution of λ would have been shifted accordingly. Such a peaked histogram is in agreement with a key prediction of ΛCDM simulations of galaxy formation: the fact that most halos exhibit the same angular momentum per unit of mass at any epoch, regardless of their total mass and their particular history of mass assembly. In this sense, the following analytic expression is known to fit the distribution of λ obtained in *N*-body simulations (see, e.g., Barnes & Efstathiou 1987; Warren et al. 1992; Gardner 2001; Bullock et al. 2001; Vitvitska et al. 2002):

$$p(\lambda)d\lambda = \frac{1}{\sqrt{2\pi}\sigma_\lambda}\exp\left[-\frac{\ln^2(\lambda/\overline{\lambda})}{2\sigma_\lambda^2}\right]\frac{d\lambda}{\lambda}. \quad (12)$$

In particular, Mo et al. (1998) adopt $\overline{\lambda} = 0.05$ and $\sigma_\lambda = 0.5$. Since it is a log-normal function, these values should not be understood as the mean and width of the distribution. In fact, this function peaks around $\lambda \sim 0.04$ and has a width of ∼0.05. Interestingly, the distribution of spin values of our galaxies agrees well with Equation (12). This implies that even though our sample is not representative of a complete one, to some extent it behaves as if it was with regard to λ and, by extension, to any other quantity that depends primarily on λ rather than on V_C.

6.1.2. Comparison with Observed Values

Before further proceeding with any detailed analysis, we must first verify that the values of λ and V_C that our fitting code yields for each galaxy agree with the observed ones. This comparison is not a straightforward task in the case of the spin parameter: being a model-dependent quantity, it cannot be directly measured in real galaxies in the same fashion as the rotational velocity. For instance, the scaling laws adopted by Hernandez & Cervantes-Sodi (2006) would yield somewhat smaller velocities and spins

[12] Note that, strictly speaking, this deprojection is only valid for the profiles corrected for internal extinction, which are the ones used in the fit. In the observed profiles, the difference between the inclined and face-on values would not just owe to a simple geometrical projection effect, since the interaction between starlight and dust along a different line of sight would also play a role.

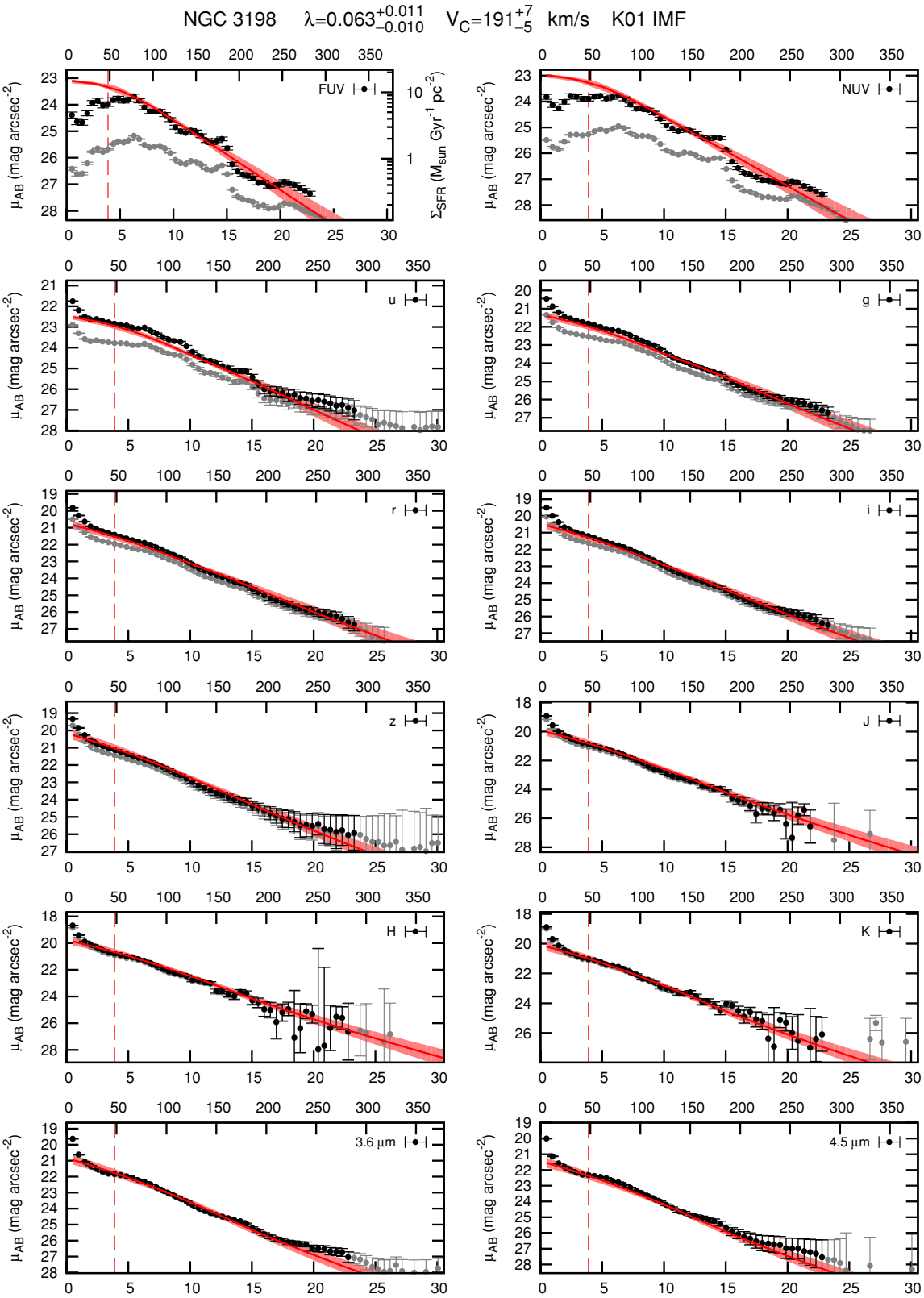

Figure 2. Best-fitting model for the Sc galaxy NGC 3198, using the K01 IMF. The gray points show the observed profiles, corrected only for Milky Way extinction, while the black ones also include a correction for the radial variation of internal extinction. Both profiles have been deprojected to their face-on values using the galaxy's morphological axis ratio. In each panel, the radius along the semimajor axis is expressed both in arcseconds (top x-axis) and in kpc (bottom x-axis). The fit is applied to those points in the extinction-corrected profiles beyond the dashed red line, in order to exclude the bulge. The red curve corresponds to the best-fitting model, and the shaded area contains all models with $\chi^2 \leqslant 2\chi^2_{\rm min}$.

(The complete figure set (84 images) is available in the online journal.)

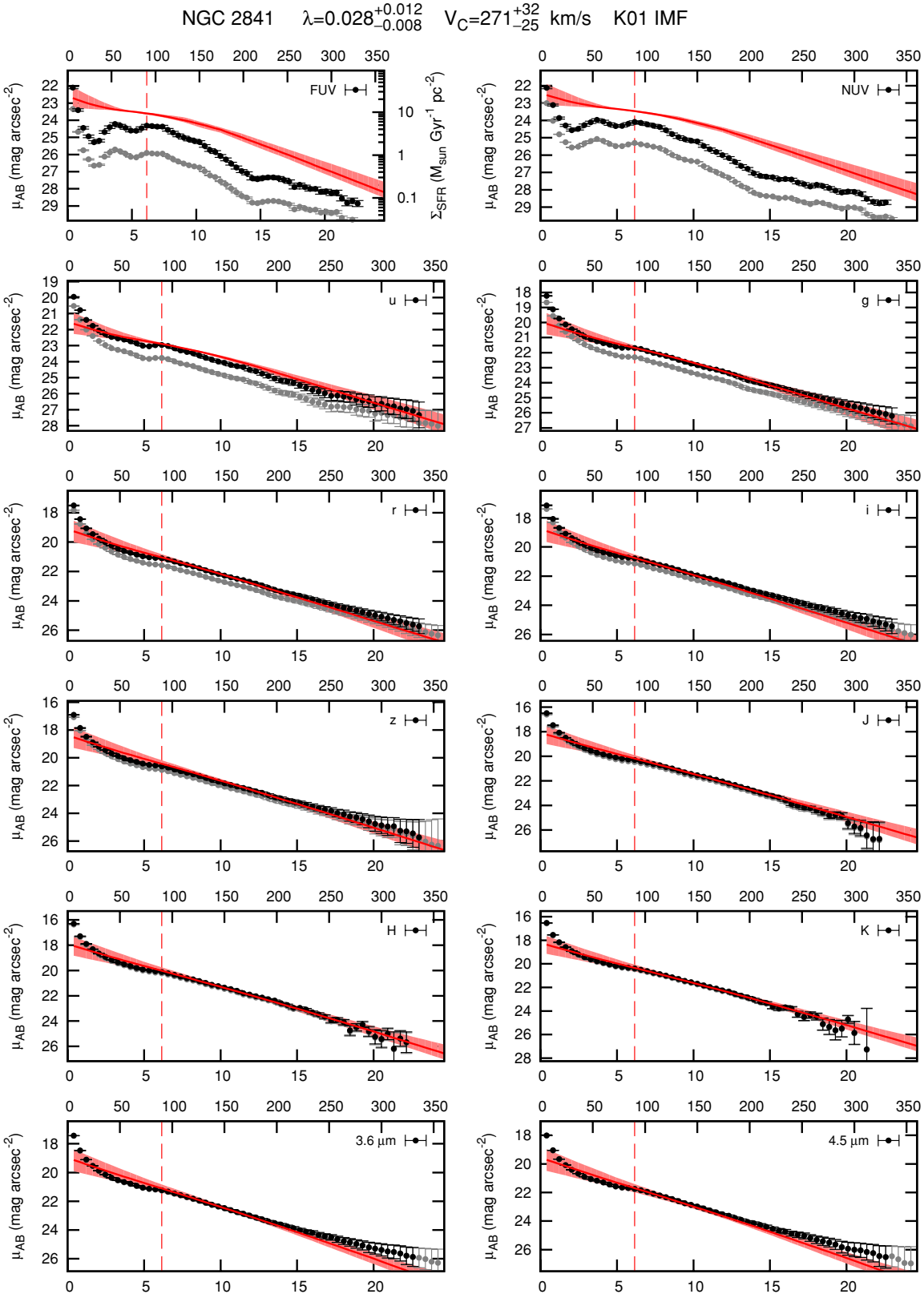

Figure 3. Same as Figure 2, but for the Sb spiral NGC 2841. The fit is excellent at all wavelengths except in the FUV and NUV bands.

than the BP00 models for galaxies more massive than the MW, and vice versa (assuming the same reference values of λ and V_C for the MW in both models). Nevertheless, as commented above, Figure 4 shows that the distribution of λ in our sample resembles the one usually found in numerical *N*-body simulations.

In order to check the accuracy of our circular velocities, in Figure 5(a) we compare the theoretical values given by the

Table 2
Model Results

Object Name	Kroupa et al. (1993) IMF				Kroupa (2001) IMF				dR_d/dt	$\frac{R_d(z=0)}{R_d(z=1)}$
	λ	V_C (km s^{-1})	Metallicity at $r = 0$	Gradient (dex kpc^{-1})	λ	V_C (km s^{-1})	Metallicity at $r = 0$	Gradient (dex kpc^{-1})	(kpc Gyr^{-1})	
(1)	(2)	(3)	(4)	(5)	(6)	(7)	(8)	(9)	(10)	(11)
NGC 0024	$0.066^{+0.015}_{-0.014}$	100^{+5}_{-5}	$8.92^{+0.08}_{-0.07}$	$-0.118^{+0.014}_{-0.015}$	$0.067^{+0.015}_{-0.014}$	98^{+5}_{-5}	$9.49^{+0.09}_{-0.08}$	$-0.128^{+0.016}_{-0.017}$	0.029	1.14
NGC 0337	$0.037^{+0.011}_{-0.010}$	169^{+9}_{-6}	$9.26^{+0.09}_{-0.12}$	$-0.085^{+0.014}_{-0.009}$	$0.036^{+0.013}_{-0.010}$	165^{+14}_{-9}	$9.87^{+0.10}_{-0.10}$	$-0.086^{+0.011}_{-0.009}$	0.052	1.26
NGC 0628	$0.057^{+0.014}_{-0.012}$	208^{+12}_{-11}	$9.17^{+0.11}_{-0.11}$	$-0.046^{+0.009}_{-0.012}$	$0.055^{+0.012}_{-0.011}$	199^{+12}_{-10}	$9.84^{+0.07}_{-0.06}$	$-0.057^{+0.008}_{-0.008}$	0.069	1.19
NGC 0925	$0.081^{+0.027}_{-0.011}$	163^{+11}_{-17}	$8.72^{+0.29}_{-0.11}$	$-0.042^{+0.013}_{-0.023}$	$0.095^{+0.020}_{-0.016}$	152^{+16}_{-10}	$9.50^{+0.07}_{-0.07}$	$-0.060^{+0.011}_{-0.010}$	0.050	1.11
NGC 1097	$0.057^{+0.021}_{-0.017}$	257^{+20}_{-15}	$9.32^{+0.07}_{-0.09}$	$-0.036^{+0.005}_{-0.004}$	$0.056^{+0.021}_{-0.017}$	256^{+22}_{-17}	$9.94^{+0.09}_{-0.11}$	$-0.041^{+0.006}_{-0.005}$	0.086	1.18
NGC 1512	$0.056^{+0.013}_{-0.012}$	144^{+9}_{-6}	$9.10^{+0.07}_{-0.07}$	$-0.078^{+0.009}_{-0.008}$	$0.058^{+0.017}_{-0.014}$	141^{+8}_{-7}	$9.68^{+0.10}_{-0.10}$	$-0.085^{+0.012}_{-0.010}$	0.047	1.18
NGC 1566	$0.052^{+0.022}_{-0.017}$	247^{+23}_{-18}	$9.33^{+0.07}_{-0.09}$	$-0.040^{+0.008}_{-0.007}$	$0.049^{+0.018}_{-0.014}$	242^{+23}_{-16}	$9.96^{+0.08}_{-0.10}$	$-0.048^{+0.007}_{-0.006}$	0.080	1.20
NGC 2403	$0.052^{+0.009}_{-0.008}$	121^{+4}_{-4}	$9.05^{+0.05}_{-0.05}$	$-0.102^{+0.010}_{-0.010}$	$0.051^{+0.009}_{-0.008}$	116^{+4}_{-5}	$9.64^{+0.06}_{-0.06}$	$-0.117^{+0.010}_{-0.010}$	0.037	1.19
NGC 2841	$0.027^{+0.011}_{-0.007}$	276^{+31}_{-27}	$9.41^{+0.02}_{-0.04}$	$-0.039^{+0.005}_{-0.004}$	$0.028^{+0.012}_{-0.008}$	271^{+32}_{-25}	$10.04^{+0.03}_{-0.05}$	$-0.046^{+0.005}_{-0.004}$	0.063	1.22
NGC 2976	$0.030^{+0.007}_{-0.005}$	76^{+2}_{-2}	$9.04^{+0.06}_{-0.05}$	$-0.202^{+0.024}_{-0.020}$	$0.033^{+0.007}_{-0.006}$	75^{+2}_{-2}	$9.62^{+0.05}_{-0.04}$	$-0.219^{+0.025}_{-0.017}$	0.021	1.26
NGC 3049	$0.082^{+0.028}_{-0.026}$	144^{+34}_{-17}	$8.95^{+0.08}_{-0.39}$	$-0.059^{+0.058}_{-0.025}$	$0.091^{+0.037}_{-0.031}$	150^{+56}_{-24}	$9.50^{+0.10}_{-0.04}$	$-0.058^{+0.025}_{-0.032}$	0.049	1.11
NGC 3031	$0.033^{+0.009}_{-0.009}$	199^{+17}_{-9}	$9.35^{+0.05}_{-0.08}$	$-0.068^{+0.007}_{-0.005}$	$0.028^{+0.014}_{-0.008}$	203^{+24}_{-18}	$10.00^{+0.06}_{-0.11}$	$-0.076^{+0.008}_{-0.005}$	0.055	1.27
NGC 3184	$0.041^{+0.014}_{-0.010}$	148^{+12}_{-6}	$9.17^{+0.11}_{-0.10}$	$-0.081^{+0.013}_{-0.018}$	$0.045^{+0.014}_{-0.013}$	145^{+8}_{-7}	$9.75^{+0.11}_{-0.08}$	$-0.088^{+0.013}_{-0.015}$	0.048	1.22
NGC 3198	$0.061^{+0.009}_{-0.010}$	198^{+6}_{-6}	$9.12^{+0.10}_{-0.10}$	$-0.049^{+0.007}_{-0.007}$	$0.063^{+0.011}_{-0.010}$	191^{+7}_{-5}	$9.78^{+0.06}_{-0.06}$	$-0.057^{+0.005}_{-0.004}$	0.066	1.17
IC 2574	$0.141^{+0.030}_{-0.021}$	103^{+21}_{-16}	$8.52^{+0.08}_{-0.08}$	$-0.075^{+0.023}_{-0.022}$	$0.144^{+0.037}_{-0.026}$	98^{+26}_{-18}	$9.03^{+0.10}_{-0.10}$	$-0.081^{+0.029}_{-0.029}$	0.027	1.06
NGC 3351	$0.037^{+0.011}_{-0.009}$	197^{+10}_{-9}	$9.32^{+0.06}_{-0.09}$	$-0.065^{+0.010}_{-0.007}$	$0.038^{+0.012}_{-0.011}$	193^{+14}_{-10}	$9.92^{+0.09}_{-0.08}$	$-0.069^{+0.009}_{-0.009}$	0.061	1.24
NGC 3521	$0.031^{+0.012}_{-0.009}$	226^{+26}_{-17}	$9.37^{+0.04}_{-0.06}$	$-0.053^{+0.006}_{-0.006}$	$0.031^{+0.015}_{-0.011}$	224^{+32}_{-20}	$10.00^{+0.06}_{-0.10}$	$-0.061^{+0.006}_{-0.006}$	0.062	1.25
NGC 3621	$0.032^{+0.008}_{-0.007}$	161^{+8}_{-9}	$9.30^{+0.07}_{-0.09}$	$-0.102^{+0.012}_{-0.009}$	$0.031^{+0.008}_{-0.007}$	156^{+12}_{-7}	$9.91^{+0.09}_{-0.08}$	$-0.105^{+0.011}_{-0.011}$	0.048	1.29
NGC 3627	$0.030^{+0.010}_{-0.007}$	219^{+21}_{-12}	$9.35^{+0.03}_{-0.04}$	$-0.053^{+0.006}_{-0.007}$	$0.032^{+0.009}_{-0.008}$	215^{+20}_{-13}	$9.98^{+0.04}_{-0.06}$	$-0.061^{+0.005}_{-0.004}$	0.061	1.25
NGC 3938	$0.045^{+0.013}_{-0.012}$	157^{+10}_{-10}	$9.15^{+0.13}_{-0.16}$	$-0.079^{+0.021}_{-0.020}$	$0.046^{+0.014}_{-0.013}$	149^{+8}_{-5}	$9.75^{+0.10}_{-0.08}$	$-0.084^{+0.014}_{-0.014}$	0.049	1.22
NGC 4236	$0.127^{+0.017}_{-0.018}$	118^{+8}_{-8}	$8.65^{+0.07}_{-0.06}$	$-0.067^{+0.010}_{-0.011}$	$0.125^{+0.020}_{-0.019}$	113^{+11}_{-9}	$9.19^{+0.08}_{-0.07}$	$-0.074^{+0.013}_{-0.013}$	0.033	1.07
NGC 4254	$0.029^{+0.014}_{-0.009}$	239^{+30}_{-21}	$9.38^{+0.03}_{-0.06}$	$-0.047^{+0.006}_{-0.005}$	$0.028^{+0.014}_{-0.008}$	240^{+31}_{-24}	$10.02^{+0.03}_{-0.08}$	$-0.055^{+0.007}_{-0.006}$	0.060	1.24
NGC 4321	$0.041^{+0.017}_{-0.013}$	295^{+22}_{-14}	$9.38^{+0.03}_{-0.04}$	$-0.030^{+0.005}_{-0.004}$	$0.040^{+0.017}_{-0.013}$	293^{+27}_{-13}	$10.03^{+0.02}_{-0.05}$	$-0.036^{+0.005}_{-0.004}$	0.084	1.20
NGC 4450	$0.041^{+0.011}_{-0.010}$	212^{+8}_{-6}	$9.31^{+0.05}_{-0.08}$	$-0.052^{+0.008}_{-0.005}$	$0.042^{+0.013}_{-0.011}$	209^{+10}_{-7}	$9.92^{+0.07}_{-0.07}$	$-0.058^{+0.008}_{-0.007}$	0.068	1.23
NGC 4536	$0.060^{+0.014}_{-0.014}$	200^{+9}_{-7}	$9.12^{+0.14}_{-0.15}$	$-0.047^{+0.011}_{-0.009}$	$0.059^{+0.017}_{-0.014}$	196^{+10}_{-9}	$9.81^{+0.10}_{-0.10}$	$-0.056^{+0.007}_{-0.006}$	0.067	1.18
NGC 4559	$0.080^{+0.010}_{-0.014}$	223^{+10}_{-7}	$9.18^{+0.07}_{-0.12}$	$-0.039^{+0.004}_{-0.004}$	$0.080^{+0.010}_{-0.013}$	220^{+9}_{-8}	$9.76^{+0.08}_{-0.06}$	$-0.043^{+0.004}_{-0.004}$	0.076	1.13
NGC 4569	$0.046^{+0.011}_{-0.009}$	256^{+14}_{-12}	$9.38^{+0.04}_{-0.05}$	$-0.042^{+0.003}_{-0.003}$	$0.048^{+0.011}_{-0.010}$	253^{+15}_{-11}	$9.99^{+0.06}_{-0.07}$	$-0.046^{+0.004}_{-0.003}$	0.082	1.20
NGC 4579	$0.029^{+0.010}_{-0.008}$	264^{+23}_{-18}	$9.38^{+0.02}_{-0.03}$	$-0.038^{+0.004}_{-0.004}$	$0.028^{+0.010}_{-0.008}$	267^{+24}_{-21}	$10.03^{+0.02}_{-0.03}$	$-0.045^{+0.005}_{-0.004}$	0.063	1.22
NGC 4625	$0.026^{+0.011}_{-0.006}$	72^{+4}_{-4}	$9.08^{+0.07}_{-0.09}$	$-0.265^{+0.070}_{-0.063}$	$0.027^{+0.014}_{-0.007}$	71^{+4}_{-5}	$9.67^{+0.09}_{-0.11}$	$-0.287^{+0.082}_{-0.073}$	0.019	1.30
NGC 4725	$0.044^{+0.016}_{-0.013}$	290^{+27}_{-15}	$9.42^{+0.04}_{-0.06}$	$-0.035^{+0.003}_{-0.003}$	$0.043^{+0.018}_{-0.015}$	288^{+36}_{-15}	$10.05^{+0.05}_{-0.09}$	$-0.041^{+0.005}_{-0.003}$	0.086	1.20
NGC 4736	$0.020^{+0.008}_{-0.001}$	146^{+8}_{-7}	$9.34^{+0.02}_{-0.07}$	$-0.125^{+0.017}_{-0.006}$	$0.020^{+0.009}_{-0.001}$	143^{+8}_{-10}	$9.96^{+0.01}_{-0.10}$	$-0.140^{+0.020}_{-0.010}$	0.036	1.35
NGC 4826	$0.020^{+0.006}_{-0.001}$	209^{+6}_{-11}	$9.39^{+0.00}_{-0.01}$	$-0.069^{+0.004}_{-0.005}$	$0.020^{+0.005}_{-0.001}$	208^{+5}_{-12}	$10.03^{+0.00}_{-0.03}$	$-0.079^{+0.004}_{-0.004}$	0.043	1.27
NGC 5033	$0.081^{+0.030}_{-0.016}$	196^{+10}_{-10}	$8.89^{+0.18}_{-0.12}$	$-0.036^{+0.009}_{-0.011}$	$0.087^{+0.024}_{-0.020}$	188^{+11}_{-8}	$9.64^{+0.11}_{-0.10}$	$-0.049^{+0.008}_{-0.007}$	0.063	1.12
NGC 5055	$0.050^{+0.016}_{-0.013}$	215^{+13}_{-9}	$9.26^{+0.08}_{-0.15}$	$-0.047^{+0.009}_{-0.006}$	$0.049^{+0.017}_{-0.013}$	212^{+15}_{-10}	$9.89^{+0.09}_{-0.09}$	$-0.054^{+0.008}_{-0.006}$	0.072	1.21
NGC 5194	$0.026^{+0.009}_{-0.006}$	239^{+21}_{-18}	$9.39^{+0.02}_{-0.04}$	$-0.051^{+0.006}_{-0.004}$	$0.025^{+0.008}_{-0.005}$	240^{+20}_{-20}	$10.03^{+0.02}_{-0.04}$	$-0.058^{+0.005}_{-0.005}$	0.054	1.24
TOL 89	$0.066^{+0.012}_{-0.011}$	117^{+8}_{-6}	$8.96^{+0.05}_{-0.05}$	$-0.092^{+0.015}_{-0.014}$	$0.070^{+0.018}_{-0.014}$	114^{+14}_{-10}	$9.51^{+0.07}_{-0.07}$	$-0.101^{+0.025}_{-0.025}$	0.035	1.14
NGC 5713	$0.020^{+0.007}_{-0.001}$	226^{+17}_{-19}	$9.40^{+0.00}_{-0.03}$	$-0.060^{+0.010}_{-0.010}$	$0.020^{+0.010}_{-0.001}$	224^{+18}_{-25}	$10.04^{+0.00}_{-0.06}$	$-0.070^{+0.012}_{-0.012}$	0.044	1.25
IC 4710	$0.078^{+0.022}_{-0.014}$	99^{+23}_{-17}	$8.84^{+0.05}_{-0.06}$	$-0.107^{+0.033}_{-0.033}$	$0.087^{+0.028}_{-0.018}$	99^{+28}_{-20}	$9.37^{+0.07}_{-0.08}$	$-0.110^{+0.042}_{-0.038}$	0.029	1.10
NGC 6946	$0.030^{+0.008}_{-0.006}$	189^{+12}_{-10}	$9.34^{+0.02}_{-0.06}$	$-0.073^{+0.012}_{-0.009}$	$0.029^{+0.008}_{-0.007}$	186^{+13}_{-11}	$9.95^{+0.04}_{-0.06}$	$-0.078^{+0.011}_{-0.008}$	0.053	1.28
NGC 7331	$0.059^{+0.027}_{-0.021}$	265^{+20}_{-16}	$9.33^{+0.09}_{-0.10}$	$-0.035^{+0.006}_{-0.005}$	$0.059^{+0.029}_{-0.023}$	263^{+22}_{-16}	$9.94^{+0.11}_{-0.13}$	$-0.039^{+0.008}_{-0.006}$	0.089	1.17
NGC 7552	$0.034^{+0.019}_{-0.014}$	223^{+35}_{-17}	$9.34^{+0.05}_{-0.13}$	$-0.048^{+0.007}_{-0.008}$	$0.033^{+0.020}_{-0.013}$	222^{+37}_{-19}	$9.98^{+0.05}_{-0.13}$	$-0.057^{+0.009}_{-0.006}$	0.064	1.25
NGC 7793	$0.040^{+0.009}_{-0.008}$	104^{+6}_{-5}	$9.06^{+0.06}_{-0.05}$	$-0.133^{+0.019}_{-0.017}$	$0.039^{+0.010}_{-0.009}$	101^{+5}_{-5}	$9.66^{+0.07}_{-0.07}$	$-0.153^{+0.021}_{-0.021}$	0.031	1.24

Notes. Results from the model fitting. (1) Galaxy name; (2, 6) dimensionless spin parameter; (3, 7) maximum circular velocity; (4, 8) central value of $12 + \log(O/H)$; (5, 9) radial metallicity gradient; (10) temporal growth rate of the stellar disk scale length, obtained by fitting $R_d(t)$ between $z = 1$ and $z = 0$. (11) Ratio of the stellar disk scale lengths at $z = 0$ and $z = 1$. Neither (10) nor (11) vary noticeably with the IMF.

model with the observed rotational velocities retrieved from the Lyon–Meudon Extragalactic Database[13] (LEDA; Paturel et al. 2003). The latter are determined from the width of the 21 cm hydrogen line at different levels and/or from rotation curves, usually Hα ones. The final values provided by LEDA are homogenized and corrected for inclination. In general, our theoretical values for the circular velocity are in agreement with the observed ones, which in some sense is expected, given that

[13] http://leda.univ-lyon1.fr

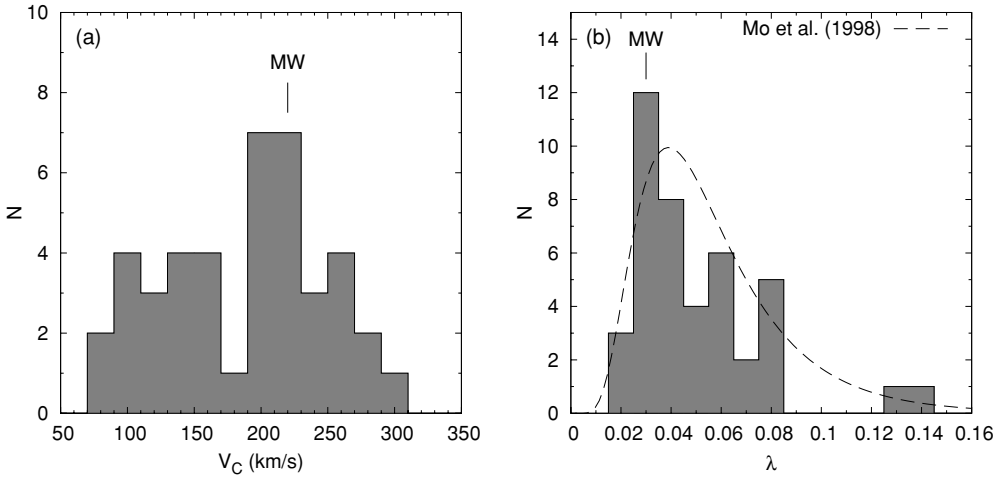

Figure 4. Distribution of the circular velocity (a) and spin (b) in our sample. The values adopted for the Milky Way ($\lambda = 0.03$ and $V_C = 220$ km s^{-1}) have been marked in both panels. The dashed curve corresponds to the probability distribution of λ proposed by Mo et al. (1998), scaled to match our histogram.

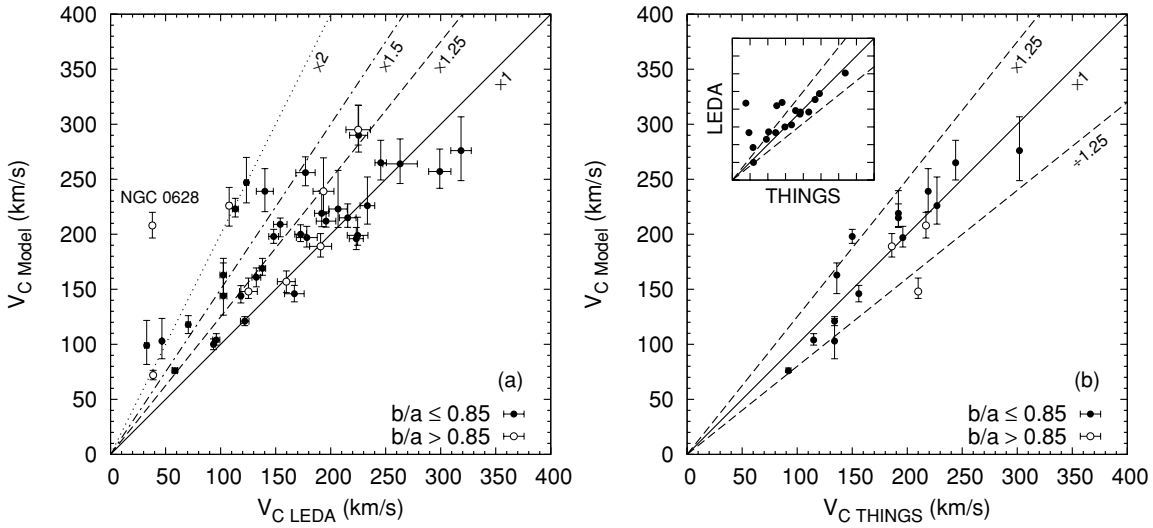

Figure 5. (a) Comparison between the circular velocities derived from the model fitting and the observed ones compiled in the LEDA database. Filled symbols correspond to galaxies with a minor to major axis ratio $b/a \leqslant 0.85$, while open ones show almost face-on galaxies with $b/a > 0.85$. (b) Same as panel (a), but using as a reference the circular velocities derived from the THINGS rotation curves. These were fitted by Leroy et al. (2008) with an analytic expression, one of whose parameters is the velocity in the flat regime of the rotation curve, which is the value we plot here. The small inset shows a comparison between the THINGS velocities and those quoted in LEDA for the same objects.

the model incorporates a Tully–Fisher (TF) relation through the adopted ΛCDM scaling laws (see discussion below).

However, for many galaxies our velocities tend to be about 25% larger than those quoted in LEDA. The most discrepant outlier in this plot is the Sc spiral NGC 0628, for which our fitting code yields $V_C = 208$ km s^{-1}, while in LEDA we find a much lower value of 38 km s^{-1}. This latter velocity is surprisingly small given that NGC 0628 has an absolute K_S-band magnitude of −21.64 mag, for which one should expect a rotational velocity of ∼175 km s^{-1} according to the TF relation (see below). The fact that this galaxy is almost face-on might introduce large uncertainties in the inclination correction, thus possibly making the LEDA velocity very uncertain for this galaxy. The open circles in Figure 5(a) show, however, that the LEDA values for many other face-on galaxies in the sample agree well with the ones obtained from the model.

There exist in the literature more accurate kinematical data for some of our galaxies. Daigle et al. (2006) and Dicaire et al. (2008) obtained Hα rotation curves for the SINGS galaxies using Fabry–Pérot interferometry. Also, the SINGS sample overlaps with The H I Nearby Galaxies Survey (THINGS; Walter et al. 2008), for which H I rotation curves were derived by de Blok et al. (2008). Here we make use of the results of Leroy et al. (2008), who parameterized the rotation curves of the THINGS galaxies with the following analytical expression:

$$v_{\rm rot}(r) = v_{\rm flat}[1 - \exp(-r/l_{\rm flat})], \quad (13)$$

where $v_{\rm rot}$ is the circular rotational velocity at a radius r, $v_{\rm flat}$ is the asymptotic velocity where the rotation curve is flat, and $l_{\rm flat}$ is the radial scale length over which $v_{\rm flat}$ is reached. Leroy et al. (2008) derived $v_{\rm flat}$ and $l_{\rm flat}$ from the high-resolution rotation curves presented in de Blok et al. (2008), as well as from the first moment maps for those low-inclination galaxies not included in de Blok et al. (2008).

In Figure 5(b), we compare the circular velocities derived from the model fitting with the $v_{\rm flat}$ values computed by Leroy et al. (2008), for the 17 galaxies we have in common. Contrary to what happens with the LEDA velocities in Figure 5(a), no systematic shift appears. Our velocities are within 20%–25% from

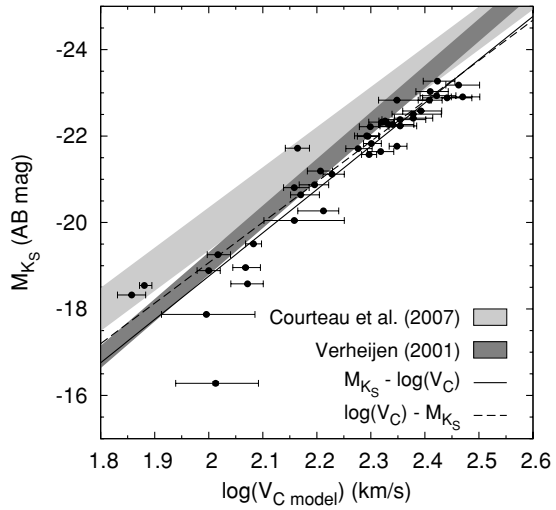

Figure 6. Absolute K_S-band magnitude of our galaxies as a function of the circular velocity of the corresponding best-fitting model. The absolute magnitudes have been derived from the asymptotic values and are corrected for internal extinction. The shaded bands correspond to the empirical TF relations of Verheijen (2001) and Courteau et al. (2007). The width of the bands shows the observed 1σ scatter of those fits. The solid and dashed lines show direct and reverse linear fits to our data, respectively.

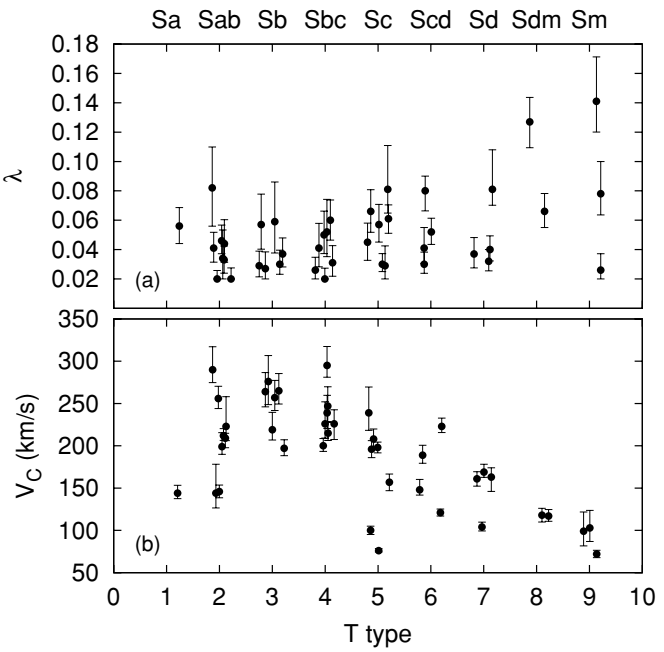

Figure 7. Dependence of (a) the spin parameter and (b) the circular velocity on the morphological type T. Given that the T types are integer values, small random horizontal offsets have been applied for the sake of clarity.

the THINGS ones. What is more, this scatter is uncorrelated with the one between the predicted and observed photometric profiles. The velocities quoted in LEDA for some galaxies in the sample of Leroy et al. (2008) tend to be lower than the values derived by those authors, and part of the discrepancy seems to be associated with differences in the corrections for inclination. Given the exquisite quality of the THINGS data and the homogeneity in the derivation of the rotation curves, we conclude that most of the systematic offset seen in Figure 5(a) is likely an issue of the LEDA values.

Another way to check the validity of our model rotational velocities consists of trying to reproduce the TF relation (Tully & Fisher 1977). This tight empirical relation links the intrinsic luminosity of a galaxy with the amplitude of its rotation curve. The former quantity traces the stellar mass, while the latter probes the total gravitational mass. Therefore, any successful model of disk evolution must be able to reproduce this observed correlation. From an observational point of view, numerous studies have shown how the slope and zero point of the TF relation vary with wavelength in the optical and near-IR, mainly due to changes in the mass-to-light ratio, together with extinction if it is not properly accounted for (Bell & de Jong 2001; Courteau et al. 2007; Pizagno et al. 2007; Blanton & Moustakas 2009).

The scaling laws adopted by BP00 imprint a built-in TF relation in the models through Equation (4). However, once star formation is implemented in a self-consistent way, the resulting slope and zero point of the TF relation might vary with wavelength due to changes in the mass-to-light ratio (see also Ferreras & Silk 2001). When comparing the TF relation resulting from the models with several empirical ones in the I band from different authors, BP00 found a good agreement, although their theoretical TF relation yielded somewhat larger velocities for a given absolute I-band magnitude.

In Figure 6, we plot the K_S-band absolute magnitude of our galaxies as a function of the circular velocity resulting from the model fitting. The absolute magnitudes were computed from the asymptotic values presented in Paper I and were corrected for internal extinction from the global TIR/UV ratio as described above. The resulting median extinction in the K_S band is just $\sim$0.03 mag. We compare our results with the empirical K_S-band TF fits of Verheijen (2001) and Courteau et al. (2007). The model TF relation lies slightly below the observed ones, with values of V_C roughly 0.05–0.1 dex larger for a given absolute magnitude, especially for the most massive galaxies. This translates into a relative offset of 10%–20%, which is much lower than the systematic scatter seen in Figure 5(a). After applying a direct and a reverse weighted linear fit to our data points, the following relations are obtained:

$$M_{K_S} = 1.3 \pm 1.4 - (10.01 \pm 0.60) \log V_C \quad (\mathrm{rms} = 0.61\ \mathrm{mag}) \tag{14}$$

$$\log V_C = -0.04 \pm 0.10 - (0.1069 \pm 0.0049) M_{K_S} \quad (\mathrm{rms} = 0.068\ \mathrm{dex}), \tag{15}$$

where M_{K_S} is expressed in AB magnitudes and V_C in km s^{-1}. Here we rely on the K_S band rather than on optical ones in order to minimize the effects of internal extinction, but comparisons between models and observations at other wavelengths can be found in BP00.

6.1.3. Trends Along the Hubble Sequence

It is illustrative to discuss whether the derived values of λ and V_C depend on the morphological type. In Figure 7, we plot the model parameters as a function of the Hubble type. The rotational velocity is clearly correlated with the morphology of the galaxies, with early-type disks rotating faster—and hence being more massive—than late-type ones (Bosma 1978; Roberts 1978; Rubin et al. 1985). However, there is no apparent trend between the spin parameter and the Hubble type, except maybe an increased scatter in Sdm–Sm galaxies.

Although the fact that the Hubble type does not seem to depend on the spin parameter might look surprising at first glance, it supports the findings of numerical simulations.

The number density of galaxies per velocity interval can be parameterized with a generalized form of the Schechter function, resulting from the combination of the luminosity function and the TF relation at a given band (Gonzalez et al. 2000). This distribution is obviously monotonic, with massive disks being rather scarce compared to low-mass ones. Given that V_C depends on the Hubble type, the probability distribution of λ would also be monotonic if this parameter was also correlated with the morphological type. However, we have seen that numerical *N*-body simulations conclude that most halos usually exhibit the same "universal" spin value $\lambda \sim 0.04$ quite irrespective of their mass. Therefore, the lack of correlation between λ and the Hubble type agrees with this result.

6.2. Potential Sources of Systematic Errors and Discrepancies in the UV

In this section, we will explore different issues that could potentially introduce biases in our results. We will pay special attention to those mechanisms that could be responsible of the excess in the UV luminosity predicted by the model in early-type disks (see Figure 3).

6.2.1. Inclination

After the profiles have been corrected for internal extinction, they are also deprojected prior to fitting them with the models. Correcting for inclination modifies the overall surface brightness level, so the resulting values of λ and V_C could be potentially affected by the precise value of the inclination angle. For consistency with the way in which the surface photometry was done, the deprojection was done by means of the observed axial ratio, $q = b/a$, so that $\cos i = q$. However, if disks are modeled as oblate spheroids, then the inclination angle can be corrected for the effects of the intrinsic thickness of the disk:

$$\cos^2 i' = \left(q^2 - q_0^2\right)\left(1 - q_0^2\right)^{-1}. \quad (16)$$

Here q_0 is the intrinsic axial ratio of the disk when observed edge-on. It is customary to assume a constant value of $q_0 \simeq 0.2$ (see, e.g., Courteau et al. 2007), although some authors argue that this value could decrease toward $q_0 \simeq 0.1$ in late-type spirals (Haynes & Giovanelli 1984; Dale et al. 1997). Taking into account the thickness of the disk slightly increases the inclination angle. As a result, the surface brightness μ' deprojected via Equation (16) is fainter than the value μ deprojected assuming $\cos i = q$:

$$\Delta\mu = \mu' - \mu = -2.5 \log \frac{\cos i'}{\cos i} = -2.5 \log \sqrt{\frac{1 - (q_0/q)^2}{1 - q_0^2}}. \quad (17)$$

It can be seen that $\Delta\mu$ lies well below 0.01 mag for $i < 50°$. At the largest inclination angles in our sample ($i \simeq 80°$ for a couple of objects) the offset in the surface brightness reaches 0.2 mag. By inspecting the output profiles of the BP00 models, we determined that $\Delta\mu \simeq 0.2$ mag corresponds to a decrease of just 10 km s^{-1} in V_C with respect to the case in which the disk thickness is ignored. The spin parameter may increase slightly to compensate for the decrease in the radial scale length due to the lower circular velocity (see Figure 1).

The most inclined spirals in our sample are NGC 0024 (Sc; $b/a = 0.22$) and NGC 7331 (Sb; $b/a = 0.35$). Our fitting code yields $V_C = 93^{+6}_{-5}$ km s^{-1} and $\lambda = 0.071^{+0.019}_{-0.015}$ for NGC 0024, if we assume that $q_0 = 0.13$ (Dale et al. 1997), whereas we get $V_C = 98^{+5}_{-5}$ km s^{-1} and $\lambda = 0.067^{+0.015}_{-0.014}$ when $q_0 = 0$. As for NGC 7331, we obtain $V_C = 250^{+19}_{-13}$ km s^{-1} and $\lambda = 0.064^{+0.026}_{-0.024}$ when assuming $q_0 = 0.20$ (Dale et al. 1997), whereas ignoring the thickness leads to $V_C = 263^{+22}_{-16}$ km s^{-1} and $\lambda = 0.059^{+0.029}_{-0.023}$. Therefore, employing a non-zero value of q_0 in disks close to edge-on leads to differences of merely $\sim$5% in both λ and V_C, which lie within the estimated uncertainties. The vast majority of the galaxies in our sample are not so inclined as the two extreme examples discussed here, so whether or not the disk thickness is included has an entirely negligible impact in the model parameters.

6.2.2. Dust Attenuation

Inaccuracies in the internal extinction correction might be responsible for the large offset between the observed and predicted UV profiles that we find in some disks. As explained in Section 4, we first compute A_{FUV} and A_{NUV} from the TIR/FUV and TIR/NUV ratios, respectively. The extinction in the optical and near-IR bands is then derived from A_{NUV} assuming a sandwich geometry and an MW-like extinction curve.

By means of radiative transfer models, several studies (Buat & Xu 1996; Meurer et al. 1999; Gordon et al. 2000; Witt & Gordon 2000; Buat et al. 2005) have shown that the TIR/UV ratio constitutes a robust proxy for the internal extinction in galaxies. In particular, it appears to be quite insensitive to the relative distribution of stars and dust and to the extinction curve (see, e.g., Figure 12(b) in Witt & Gordon 2000). In the particular case of the recipes of Cortese et al. (2008)—the ones employed here to compute A_{FUV} and A_{NUVM}—variations in the dust geometry and the extinction law modify the derived attenuations by less than 0.2 mag (see their Figure 9).

When computing the extinction A_λ at other wavelengths by extrapolating from A_{NUV}, our particular choice of dust geometry and extinction curve will indeed play a role. However, in the case of the near-IR bands the impact will be minimal: at those wavelengths the internal extinction will be still close to zero even if the sandwich model is not appropriate or if the galaxy's extinction curve does not resemble that of the MW. In brief, for a given galaxy where the model that best fits the near-IR profiles significantly overestimates the UV ones, switching to another dust-to-stars geometry or extinction law would not fix the problem. The extinction in the UV would not vary noticeably due to the robustness of the TIR/UV ratio against these changes, and the extinction in the near-IR would remain close to zero. Variations would show up at intermediate wavelengths, in the optical range, but the model seems to match the optical profiles even in those cases where it fails in the UV (Figure 3).

Another aspect of the internal extinction correction that should be taken into account is the relative role of young and old stars in heating the dust. In galaxies with low SFR per unit of mass (specific SFR, or sSFR), the contribution of old stars to the dust heating will be larger than in more actively star-forming galaxies, thus biasing the energy balance argument on which the TIR/UV method relies. Therefore, a given calibration between TIR/UV and A_{UV} that is valid for late-type spirals will overestimate the actual extinction in early-type ones.

In Paper II, we used two different recipes to derive attenuation profiles for the SINGS galaxies: the calibration of Buat et al. (2005), which does not account for the varying extra dust heating due to old stars, and the age-dependent calibration of Cortese et al. (2008), the one finally adopted here. The difference between both prescriptions is negligible in disk-dominated galaxies. However, in S0/a–Sab galaxies and the bulges of

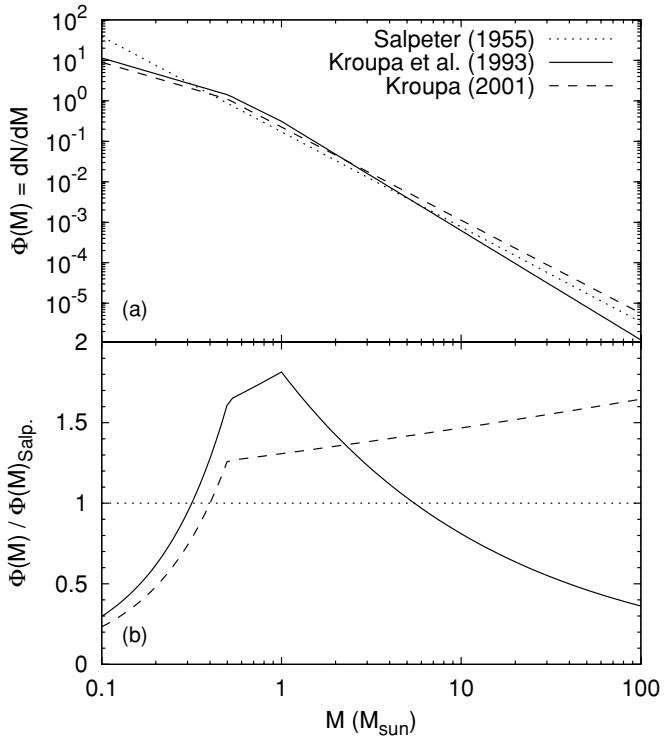

Figure 8. (a) IMFs of Salpeter (1955), Kroupa et al. (1993), and Kroupa (2001), normalized to a total stellar mass of 1 $M_\odot$. (b) Ratio of the K93 and K01 IMFs to the Salpeter one.

later-type spirals, the method of Buat et al. (2005) yields extinction values ∼0.5 mag larger than those obtained with the recipes of Cortese et al. (2008), since the extra contribution of old stars to the dust heating is not "removed" in the former. Therefore, using the calibration of Buat et al. (2005) would bring the observed profiles closer to the model predictions. However, this better agreement would be achieved at the expense of using an extinction recipe that is known not to be valid in early-type spirals. Nevertheless, the difference of ∼0.5 mag is not large enough to account for the UV discrepancies found in many of our disks.

6.2.3. Initial Mass Function

The IMF, usually denoted as $\Phi(M)$, indicates the number of stars in the mass interval M to $M + dM$ formed in a given burst. The classical IMF of Salpeter (1955) consists of a single power law across the entire stellar mass range, $\Phi(M) \propto m^{-\alpha}$, where $\alpha = 2.35$. In this work, we have used two grids of models with the K93 and K01 IMFs, which are multi-sloped:

$$\begin{aligned} 0.1 \leqslant M/M_\odot < 0.5 \qquad & \alpha_{\rm K93} = 1.3;\ \alpha_{\rm K01} = 1.3 \\ 0.5 \leqslant M/M_\odot < 1.0 \qquad & \alpha_{\rm K93} = 2.2;\ \alpha_{\rm K01} = 2.3 \\ 1.0 \leqslant M/M_\odot \qquad & \alpha_{\rm K93} = 2.7;\ \alpha_{\rm K01} = 2.3. \end{aligned} \quad (18)$$

These IMFs are shown in Figure 8, where they have been normalized such that

$$\int_{M_{\rm min}}^{M_{\rm max}} \Phi(M) M dM = 1, \quad (19)$$

where the integration is carried out between $M_{\rm min} = 0.1\ M_\odot$ and $M_{\rm max} = 100\ M_\odot$.[14] The K01 IMF has more short-lived massive stars for a given total stellar mass, so it yields larger UV fluxes for the same near-IR and optical luminosities. Therefore, choosing one IMF or another obviously affects the ability of the model to simultaneously fit all the multi-wavelength profiles.

[14] Note that while the Salpeter IMF is normally assumed to hold over the range 0.1–100 $M_\odot$, the original Salpeter (1955) study only included stars in the range 0.4–10 $M_\odot$.

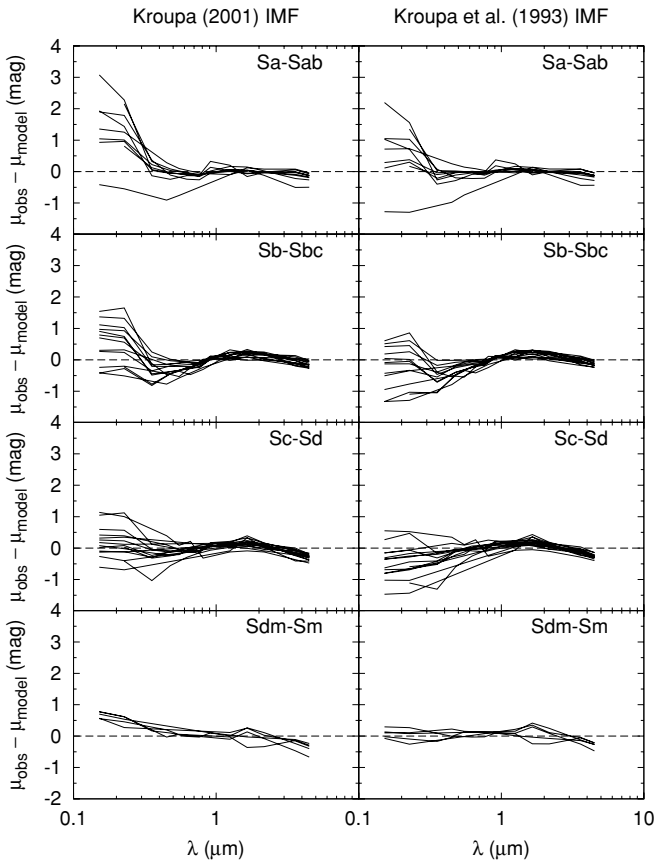

Figure 9. Average difference between the observed and model surface brightness profiles for each galaxy at different wavelengths. The average offset was computed within the radial range used during the fitting procedure. Note that the "observed" profiles are already corrected for internal extinction.

In order to quantify the discrepancy between the model predictions and the actual profiles, for each galaxy and wavelength we have computed the average difference between the observed and model surface brightness within the radial range considered in the fitting procedure. "Observed" is used here in contrast to "model," but the "observed" profiles we consider are of course those corrected from internal extinction. The results are shown in Figure 9 for each IMF and morphological type.

It is clear that neither IMF provides a satisfactory fit at all wavelengths and for all morphological types simultaneously. The largest discrepancies are found in the UV range, as expected. The K01 IMF yields an excellent fit for most Sc–Sd spirals, as well as for some Sb–Sbc ones. However, it significantly overestimates the UV flux in early-type disks. The K93 IMF, on the other hand, partly mitigates the problem in some Sb–Sbc galaxies, but the perfect agreement between model and observations found in Sc–Sd disks is partially lost. Very late type disks, however, are better fitted with the K93 IMF than with the K01 one.

Elucidating whether a varying IMF is the actual reason behind these discrepancies is not straightforward, as other mechanisms could introduce similar systematic biases in the UV profiles. For instance, the UV bands can be affected by variations in the SFR taking place on timescales of ∼100 Myr, whereas

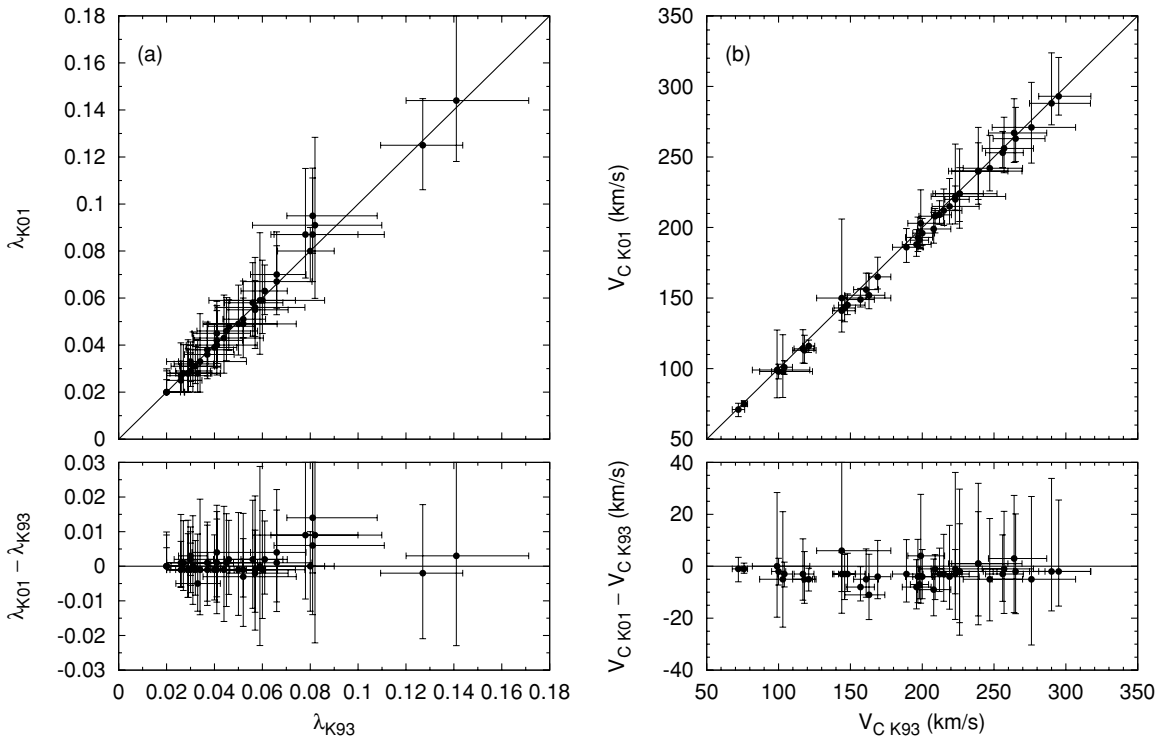

Figure 10. Comparison of the values of the spin parameter and circular velocities obtained when using the IMFs of Kroupa et al. (1993) and Kroupa (2001). The solid line shows the corresponding 1:1 relations.

the u band will respond to variations over ∼500 Myr. This increase in the characteristic timescale between the UV and optical bands seems to be indeed rather sharp (S. Boissier et al. 2011, in preparation). Therefore, short-scale SFR variations could partly explain why the discrepancies between the observed and predicted profiles drop abruptly between the UV and u bands. Also, the calibration of the stellar atmospheres used in the spectral synthesis models might not be as accurate in the UV as they are in the optical, since observations of stars in the UV are not so easily accessible.

It has been argued that the so-called Integrated Galactic Initial Mass Function, which takes into account the clustered nature of star formation, varies among galaxies, leading to a scarcity of massive stars in galaxies with low global SFRs (Weidner & Kroupa 2005). Krumholz & McKee (2008) brought forward a physical explanation to the apparent dearth of massive stars in low-density regions, arguing that gas column densities of at least 1 g cm^{-2} are required to halt cloud fragmentation and produce massive stars. Stochastic formation of high-mass stars might also play a role in galaxies with very low levels of star formation (Lee et al. 2009).

These mechanisms have been proposed to explain the observed discrepancies between the UV and Hα-derived SFRs in dwarf galaxies (Pflamm-Altenburg et al. 2007, 2009; Lee et al. 2009) and in LSBs (Meurer et al. 2009). In this regard, even though both the K93 and K01 IMFs are canonical, it would make sense that Sdm–Sm disks are better fitted with a top-light IMF like the K93 one rather than with the K01 one. However, the effects described here seem to arise mainly in irregular galaxies with much lower levels of SF than the disks considered in this work (see also Boselli et al. 2009). In any case, we cannot appeal to these mechanisms to explain the discrepancies in the UV bands found in early-type disks.

Nevertheless, it is worth asking whether our particular choice of IMF affects the results of the fitting. Thanks to our two-step fitting procedure, which estimates the intrinsic error of the model for each galaxy and band after a first run, the UV bands are automatically assigned a relatively large error whenever large discrepancies are found. This prevents the UV bands from biasing the fit at longer wavelengths. In Figure 10, we compare the values of λ and V_C obtained with both IMFs. The differences are obviously negligible and much smaller than the estimated uncertainties, since the fit is still excellent in the optical and near-IR bands even when it fails in the UV. Therefore, even if the very recent level of SF (either massive or total) predicted by the models for the last few hundreds of Myr is not entirely reliable, the overall star formation history across longer timescales can still be trusted.

Besides modifying the emitted UV flux, changing the IMF also has a significant impact in the resulting metallicity profiles predicted by the model. In Figure 11, we compare the central abundances and radial gradients obtained with both IMFs. Given that the K01 IMF is richer in massive stars than the K93 one, it produces more Type II supernovae and metals, leading to oxygen abundances which are ∼0.62 dex larger than those resulting from the K93 IMF. Note that the uncertainties associated with different metallicity calibrations are typically ∼0.3 dex (see Moustakas et al. 2010). The radial gradients, on the other hand, remain nearly unchanged, the K01 ones being just mildly steeper.

We must also check whether the oxygen abundance profiles predicted by the model are in agreement with the observed ones. As in Paper II, here we rely on the metallicity zero points and gradients measured by Moustakas et al. (2010), using the calibration of Kobulnicky & Kewley (2004). In Figure 12, we plot the central oxygen abundances as a function of the predicted values using both IMFs. The values computed with the K93 IMF are just 0.1 dex larger than the observed central abundances, whereas those yielded by the K01 IMF are roughly 0.7 dex larger. Such high metallicities have never been observed;

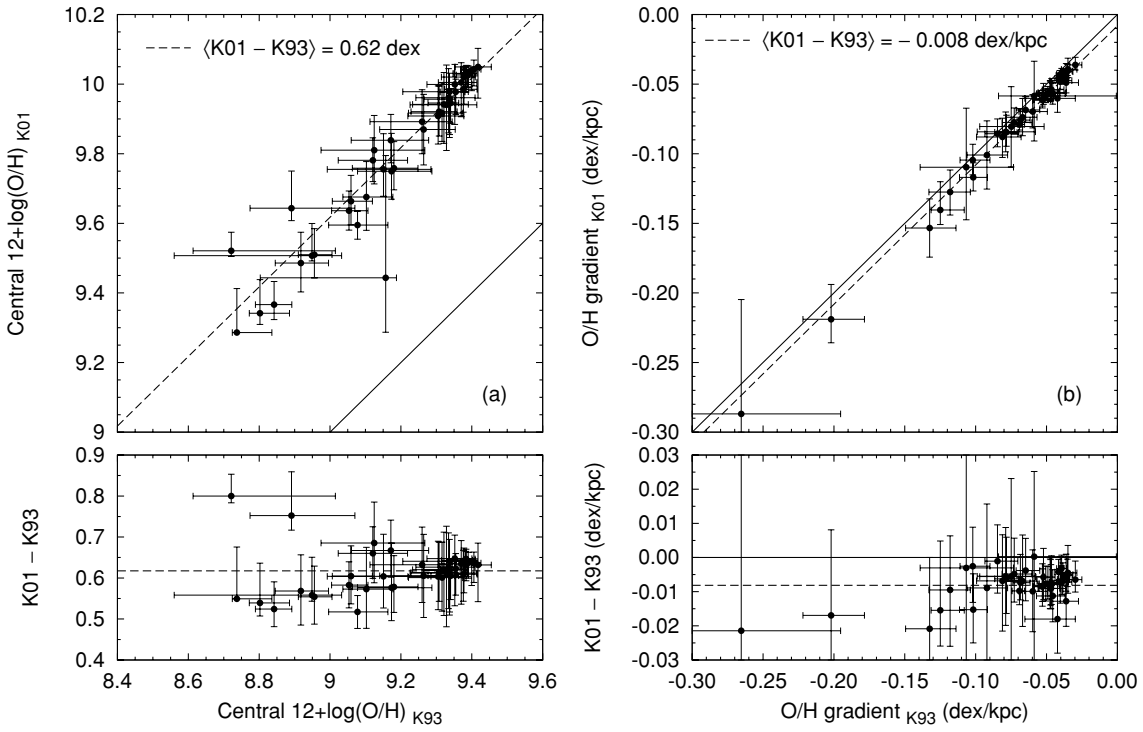

Figure 11. Comparison of the (a) central abundances and (b) gradients obtained when using the IMFs of Kroupa et al. (1993) and Kroupa (2001). The solid lines in each panel correspond to the 1:1 relation, while the dashed lines show linear fits where only the zero point has been left as a free parameter. The corresponding offset is quoted in each panel.

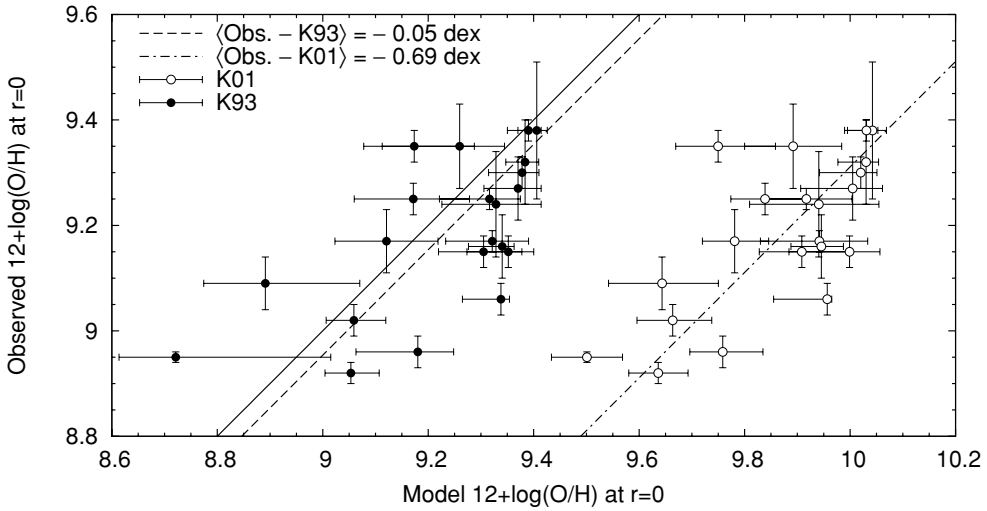

Figure 12. Comparison between the observed and predicted central abundances for those SINGS galaxies with metallicity profiles computed by Moustakas et al. (2010). The average offsets for the K93 and K01 IMFs are shown with a dashed line and a dot-dashed line, respectively, while the solid one corresponds to the line of equality.

moreover, the flat slope for massive stars of the K01 IMF would lead to a significant depletion of deuterium through astration in the solar neighborhood.

As pointed out by several authors (see, e.g., Kewley & Ellison 2008; Moustakas et al. 2010), different methods used to measure the gas-phase metallicity from observed emission-line spectra can yield largely discrepant results. Besides the calibration of Kobulnicky & Kewley (2004), Moustakas et al. (2010) also derived metallicity profiles using the calibration of Pilyugin & Thuan (2005). Both methods are based on the strong-line R_{23} parameter (Pagel et al. 1979). The empirical method of Pilyugin & Thuan (2005) is calibrated on H II regions having direct abundance measurements based on the electron temperature. The theoretical calibration of Kobulnicky & Kewley (2004), on the contrary, relies on photoionization models. The method of Pilyugin & Thuan (2005) leads to oxygen abundances ∼0.6 dex lower than those obtained with the Kobulnicky & Kewley (2004) calibration. Therefore, had we used the Pilyugin & Thuan (2005) values in Figure 12, even the metallicities predicted with the K93 IMF would be too high compared with the observed ones, and the discrepancy with the K01 IMF would be even larger than it already is. As thoroughly discussed by Moustakas et al. (2010), neither empirical nor theoretical strong-line methods are devoid of problems. On one hand, empirical methods like the Pilyugin & Thuan (2005) one might fail outside the metallicity range spanned by the H II regions used in the calibrations and

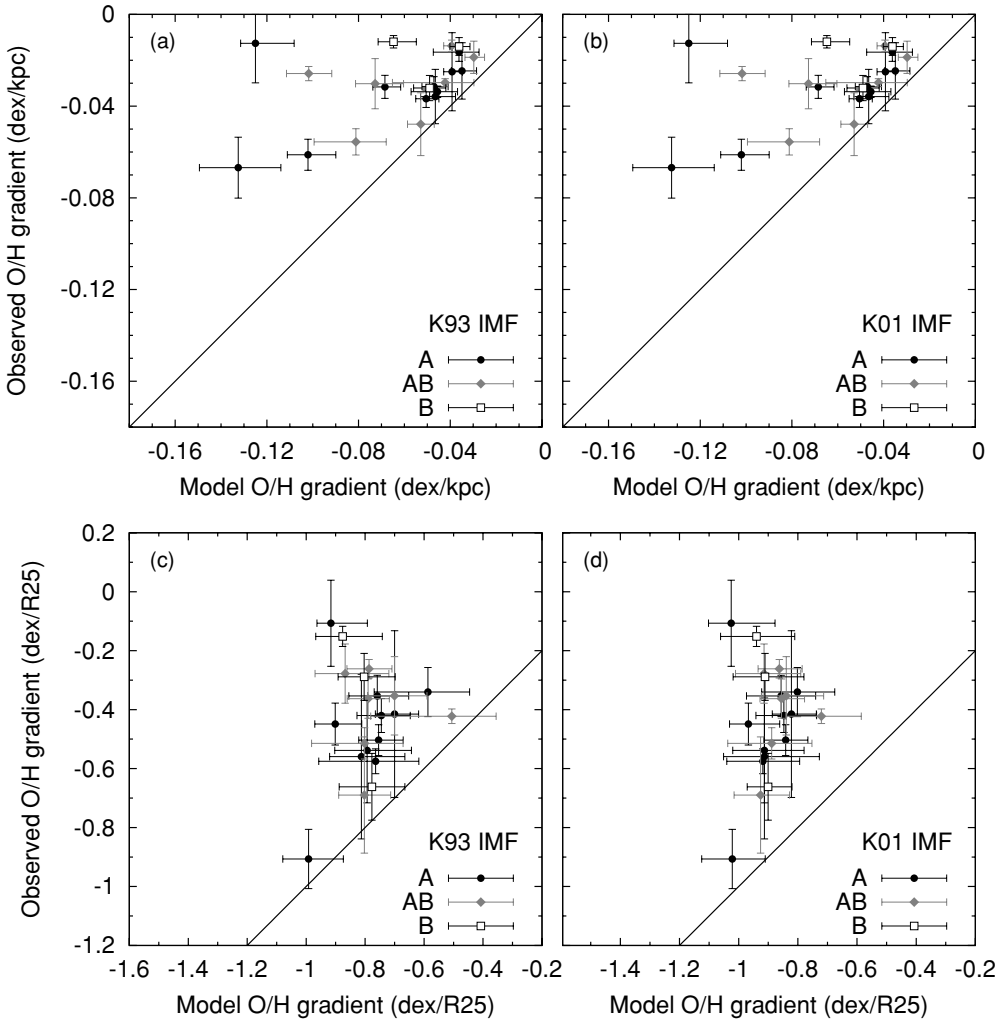

Figure 13. Comparison between the observed and predicted abundance gradients for those galaxies in the sample of Moustakas et al. (2010). Panels (a) and (b) show the gradients in units of dex kpc^{-1} for both IMFs, whereas in panels (c) and (d) the gradients are expressed in units of the optical radius R25. Galaxies are sorted out into non-barred (A), barred (B), and mixed (AB). The solid line marks the 1:1 relation in all cases.

can therefore underestimate the true abundances in the high-metallicity regime. On the other hand, theoretical methods such as the Kobulnicky & Kewley (2004) one adopt several simplifying assumptions on the properties of the gas clouds and the ionizing stars that can make the derived metallicities higher than the actual ones. The two calibrations discussed here bracket the range of abundances usually obtained with other methods, so the actual metallicities probably lie somewhere in between.

As for the radial gradients, they are plotted in Figure 13, both in units of dex kpc^{-1} (upper panels) and normalized by the optical radius R25 (lower panels). The gradients predicted by the model are always steeper than the observed ones, although for most galaxies the difference is just about $\sim$0.015 dex kpc^{-1}. When expressed in terms of the optical radius, the model predicts a roughly constant gradient of -0.8 dex/R25 for the K93 IMF, and -0.9 dex/R25 for the K01 one. This "universal" oxygen gradient, which does not depend on galaxy mass, is usually found in observations (see, e.g., Henry & Worthey 1999). However, the spread is larger than that predicted by the models, with observed gradients ranging from -1 dex/R25 to almost flat gradients. The fact that the comparison of gradients in units of dex kpc^{-1} is somewhat better than in dex/R25 is not surprising, since the former are mainly determined by the radius of the disks, which varies substantially within the sample. Therefore, the comparison between observed and model gradients in dex kpc^{-1} is more a test of the prediction of disk sizes than of abundance gradients.

Bars may induce radial gas flows that can yield shallower metallicity gradients (see, e.g., Martin & Roy 1994). Two out of the three barred galaxies in Figure 13 are among the ones with the flattest observed gradients, although the subsample considered here is obviously too small to extract any statistically significant conclusion. Recent numerical *N*-body simulations have shown that radial stellar migration can also flatten the final metallicity profiles (Roškar et al. 2008; Martínez-Serrano et al. 2009; Sánchez-Blázquez et al. 2009), although these results refer to the stellar metallicity and not to the gas-phase one.

To summarize this discussion on the IMF, most Sc–Sd spirals require the K01 IMF in order not to underestimate the UV luminosity, but at the expense of ending up with oxygen abundances much larger than the observed ones. Conversely, the K93 IMF provides a somewhat better fit for the remaining Hubble types, and is able to reproduce the correct present-day abundances. Whether the better agreement with the observed metallicities should be given a special importance is unclear, since neither the measured values nor the predicted ones are devoid of possible sources of large systematic errors. On one hand, the different existing calibrations used to compute

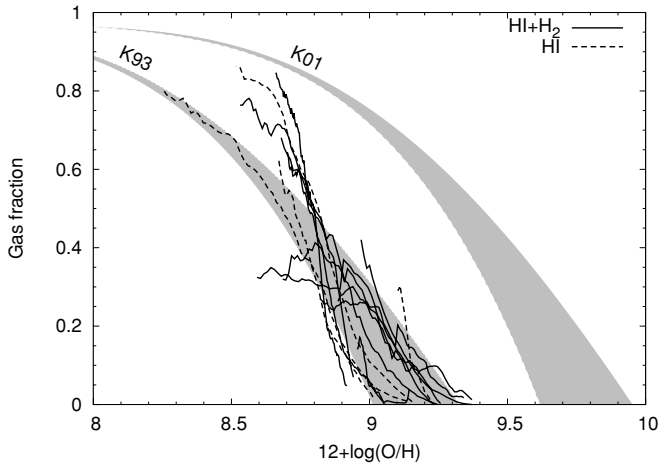

Figure 14. Trend between the gas fraction and the gas-phase oxygen abundance. The shaded bands show the model predictions for the K93 and K01 IMFs. The black lines show the observed gas fractions of our galaxies, resulting from the combination of atomic and molecular gas profiles with stellar mass ones. The latter were derived from the observed 3.6 μm profiles, adopting the M/L ratio yielded by the model at this band. Solid lines indicate those galaxies with H_2 profiles, whereas dashed ones are used when only H I profiles were available. The observed gas profiles were multiplied by 1.36 to include helium and heavy elements. The model profiles already show the total gas surface density.

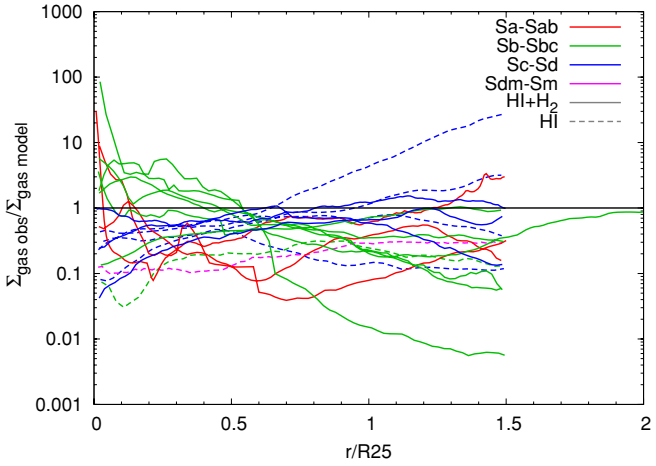

Figure 15. Ratio between the observed gas surface density and the value predicted by the model at different radii for each galaxy (see the text for details). Solid lines correspond to galaxies with both atomic and molecular gas profiles available, whereas dashed ones are used for those objects lacking CO profiles. The observed gas profiles have been multiplied by 1.36 to account for helium and heavy elements. The model profiles already include the total gas surface density.

the oxygen abundance from observed line ratios may lead to systematically different values, as explained before (Kewley & Ellison 2008; Moustakas et al. 2010). On the other hand, uncertainties in the stellar yields used in the disk evolution models will affect the predicted metallicities. Besides, we cannot neglect the possibility that the library of synthetic spectra used to compute the multi-wavelength profiles could be quite off in the UV range.

With these issues in mind, we opt for a compromise solution and adopt the K93 IMF as our default choice in this paper, otherwise stated. This choice is done without any prejudice to the K01 which, we reiterate, provides an excellent fit for many disks in our sample, especially Sc–Sd ones.

6.2.4. Gas Content and SF Efficiency

Apart from the broadband photometric profiles, the model also outputs the total gas density profiles, which can be therefore used as another observational constraint of the accuracy of the model. In particular, and continuing the discussion presented in the previous section, the gas fraction might shed some light into the disagreement in abundance gradients. The baryonic gas fraction is defined as $f_g = M_g/(M_* + M_g)$, where M_* and M_g are the stellar and gas masses, respectively. As star formation proceeds, gas is progressively consumed and transformed into stars, which later enrich the remaining gas with heavy elements. Therefore, f_g is expected to decrease with O/H, although the particular trend might depend on the presence of inflows or outflows (Boissier et al. 2001; Garnett 2002).

In Figure 14, we compare the gas fraction profiles predicted by the model with the actual ones found in our galaxies. According to the model, f_g decreases with V_C and increases with λ (Boissier et al. 2001). The shaded areas shown here cover the range of values of V_C and λ found in our sample. As for the observed quantities, the atomic gas profiles were measured on H I maps from THINGS, using the same ellipticity, position angle, and radial step as those used when computing the UV, optical and near-IR profiles. Whenever possible, we included CO profiles compiled from the literature to account for the molecular gas content. The CO profiles were converted into H_2 ones by means of a metallicity-dependent X_{CO} conversion factor (Boselli et al. 2002), using the local oxygen abundance at each galactocentric distance. Solid lines are used for those galaxies with available molecular gas profiles (although most if not all of the gas content in the outer parts is entirely atomic). Dashed lines correspond to galaxies for which only H I data were available. In all cases, we multiplied the hydrogen profiles by 1.36 to account for helium and heavy elements. Stellar mass profiles for each galaxy were derived from the 3.6 μm ones, using the M/L ratio yielded by the model, and combined with the gas profiles to obtain $f_g(r)$.

As already discussed before, the K01 IMF yields excessively large metallicities, whereas the K93 one provides a much better agreement with the observed values. While the model is successful at reproducing the observed trend, for some galaxies f_g seems to decrease faster with O/H compared to the model predictions, consistent with the observed O/H gradients being flatter than the model ones.

The gas profiles can also shed light on the discrepancy between the observed and predicted UV profiles, which may arise from differences in the amount of gas that settles onto the disk or the way it is transformed into stars. In Figure 15, we show the ratio between the gas surface density predicted by the model and the actual one for each galaxy as a function of radius. Here, we plot the model gas density obtained with the K93 IMF; the values yielded by the K01 IMF are within $\pm$20% of the ones shown here.

In the disks of Sc–Sd spirals the gas profiles predicted by the models agree with the observed ones. However, in general the model overestimates the actual gas content by a factor of $\lesssim$10, which is considerable. Does this lead to systematic differences in the emerging FUV luminosity? In Figure 16, we compare the offset between the observed and predicted FUV brightness with the corresponding observed-to-predicted gas ratio at each radius. While there is a non-negligible scatter, a clear trend is seen, in the sense that the model overestimates the FUV brightness wherever it also predicts too much gas content.

It is worth investigating whether the star formation efficiency (SFE) plays a role in driving the predicted UV profiles away

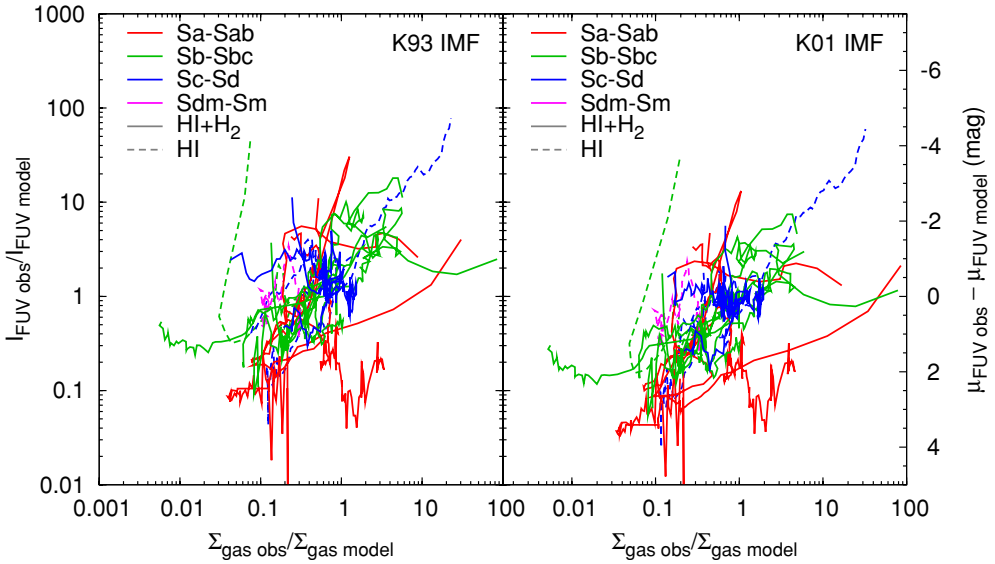

Figure 16. Observed-to-predicted gas ratio is plotted against the discrepancy between the actual UV surface brightness—already corrected for internal extinction—and the value predicted by the model. This UV discrepancy is expressed in terms of a magnitude offset (right *y*-axis) and the corresponding flux ratio (left *y*-axis). Unlike Figure 9, where this offset was averaged all over the disk, here we plot the full range of values at different galactocentric distances, so each galaxy follows a track in this plot.

from the actual ones. After all, even if the gas profiles are correctly reproduced by the model, the emitted UV light will still depend on the particular way in which the model handles the process of star formation. As explicitly stated in Equation (1), the model relies on a hybrid star formation law that combines the classical Schmidt–Kennicutt law with an orbital term (see Leroy et al. 2008 for an extensive analysis of various other laws). The value of the efficiency α in Equation (1) was chosen to reproduce the present-day observed gas fraction in nearby galaxies (Boissier et al. 2003).

Even though the efficiency α is kept constant in the models,[15] it may actually vary among galaxies or even within them. This assumption can be tested, given that α depends on the SFR density, the gas density, and the rotational velocity at each radius, all of which can be measured. In Figure 17, we plot the radial variation of α for each galaxy. The SFR profiles were computed from the extinction-corrected FUV ones, using the conversion factor of Kennicutt (1998). This recipe assumes solar metallicity, a constant SFR over the last few Myr, and a Salpeter (1955) IMF. The small ticks at the bottom right show how the profiles would shift with the K93 and K01 IMFs. The gas surface density was again obtained from THINGS and CO profiles. Finally, the circular velocity at each radius was derived from the fits of Leroy et al. (2008) to the THINGS rotation curves (Equation (13)). For the few THINGS galaxies not considered by Leroy et al. (2008), the rotation curve from the best-fitting model was used instead as a proxy for the actual one.

Figure 17 shows that, except for a few objects, α remains roughly constant with radius within most disks, although it does vary from galaxy to galaxy. The empirical values of α are consistent with or somewhat larger than the constant value assumed in the model, shown here as a horizontal line. The average scatter is nonetheless considerable, around 1 dex. There

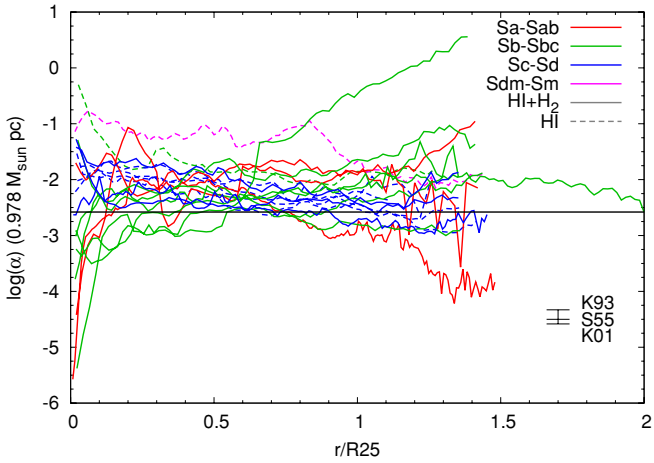

Figure 17. Empirical value of the efficiency parameter α in Equation (1) (see the text for details on how α was derived from observations). The units of α are such that $\Sigma_{\rm SFR}(r)$ is measured in $M_\odot$ pc^{-2} Gyr^{-1}, $\Sigma_{\rm gas}(r)$ in $M_\odot$ pc^{-2}, r in kpc, and $V(r)$ in km s^{-1}. The horizontal solid line marks the constant value assumed in the models (see Boissier et al. 2003). $\Sigma_{\rm SFR}(r)$ was derived from the extinction-corrected UV profiles using the recipe of Kennicutt (1998), which assumes a Salpeter (1955) IMF. The small ticks at the bottom right show how the plotted curves would shift with the K93 and K01 IMFs.

are several factors contributing to this dispersion in the measured values of α. On one hand, variations in the IMF will affect the adopted calibration for the SFR as a function of the FUV luminosity. Moreover, the assumption of a constant SFR over the last few Myr might not hold in some cases. Besides, departures from solar metallicity—both among and within galaxies—will also affect the SFR calibration. Uncertainties in the CO-to-H_2 conversion factor will modify the total gas surface density, although this is only a concern in the innermost regions. Nevertheless, part of the observed scatter likely reflects intrinsic variations of α among galaxies.

Interestingly, when plotting the observed-to-predicted UV offset as a function of the empirical values of α we do not observe any significant trend between both parameters, in contrast with

[15] Note that although α can be interpreted as the efficiency of the SFR, by star formation efficiency (SFE) one usually means the ratio of the SFR and the gas mass. In our case, $\mathrm{SFE}(t, r) = \alpha \Sigma_{\rm g}(t, r)^{0.5} V(r) r^{-1}$, so even under the assumption of a constant value of α, SFE is still a varying function of radius and time.

Figure 16, where the data cloud was clearly tilted. In other words, the UV discrepancy appears to be independent of the precise value of α, so a morphology-dependent value of α cannot account for the mismatch between the observed and theoretical UV profiles. Therefore, the bottom line of this analysis is that the discrepancies in the UV profiles of early-type disks are mainly due to an excessive amount of gas retained by the model in these galaxies, rather than to its subsequent conversion into stars.

Some of the galaxies in our sample with the largest UV discrepancies belong to the Virgo cluster or the Coma Cloud. Hydrodynamical interactions with the hot intergalactic medium or gravitational ones with other cluster members might have removed part of the gas in their disks, thus quenching the recent star formation activity (see Boselli & Gavazzi 2006 for a review). This effect would lead to significantly lower UV fluxes than those predicted by the model. In order to test whether this is actually the case, we have computed the so-called H I deficiency for the galaxies in our sample. This parameter, defined by Haynes & Giovanelli (1984), compares the observed H I mass of a galaxy with the typical H I mass of isolated field galaxies with a similar morphological type $T^{\rm obs}$ and linear optical diameter $D^{\rm obs}_{\rm opt}$:

$$\text{H I def} = \langle \log M_{\rm H\,I}(T^{\rm obs}, D^{\rm obs}_{\rm opt}) \rangle - \log M^{\rm obs}_{\rm H\,I}. \quad (20)$$

Therefore, positive H I deficiencies correspond to galaxies with lower gas contents than those of similar but isolated objects. Here we use the calibration of $M_{\rm H\,I}(T^{\rm obs}, D^{\rm obs}_{\rm opt})$ derived by Solanes et al. (1996), since it relies on a larger sample of galaxies than that used in the seminal paper by Haynes & Giovanelli (1984). Following Solanes et al. (2001), the reference H I masses for galaxies later than Sc have been computed following the prescriptions for Sc ones. The intrinsic scatter in measurements of the H I deficiency is typically $\pm$0.2–0.3 dex (Haynes & Giovanelli 1984; Solanes et al. 1996), and it is customary to assume that galaxies with deficiencies lower than 0.03–0.05 possess normal H I contents.

In Figure 18, we plot the average UV offset between the observed and predicted UV profiles as a function of the H I deficiency. The integrated H I masses of the SINGS galaxies have been taken from Draine et al. (2007). There are indeed some galaxies with simultaneously large H I deficiencies and UV offsets. In NGC 4569, NGC 4579 and NGC 4826, the model perfectly fits the optical and near-IR profiles, but it substantially overestimates the UV ones, especially in the outer regions.

NGC 4826 is an anemic spiral in the Coma 1 Cloud (van den Bergh 1976; Boselli & Gavazzi 2009). It is known to host two counter-rotating gaseous disks that possibly point toward a past merger event (Braun et al. 1992). It also exhibits a central dark lane that has earned this object the nickname "the black-eye galaxy." Its stellar component extends beyond $r \gtrsim 13$ kpc, as shown by the optical and near-IR profiles, but most of the star formation activity is currently restricted to $r \lesssim 3$ kpc, where most of the gas is located.

Something similar happens with NGC 4569 and NGC 4579, two other anemic spirals in the Virgo Cluster (van den Bergh 1976). In order to properly fit the multi-wavelength profiles of NGC 4569, Boselli et al. (2006) employed a modified version of the BP00 models in which the gas infall could be tuned to simulate starvation (by simply stopping gas infall) or ram pressure stripping (by removing gas already settled onto the disk). These authors concluded that ram pressure stripping is required to explain the truncated H I and star-forming disks of this galaxy.

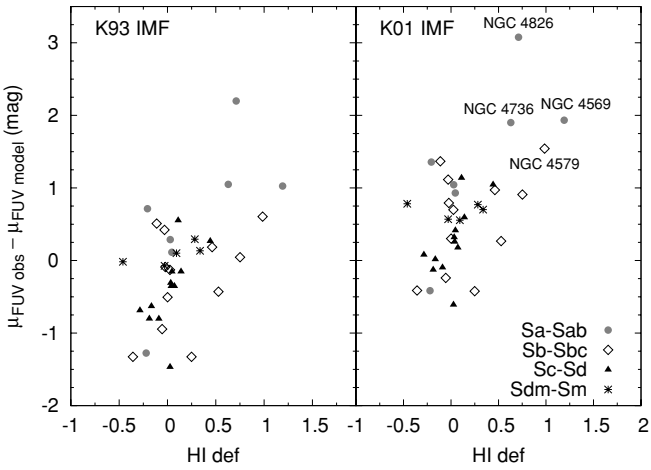

Figure 18. Offset between the observed and model UV surface brightness as a function of the H I deficiency. The latter is obtained by comparing, in logarithmic scale, the total H I mass of a given galaxy and the typical H I mass of isolated galaxies with similar morphological types and linear diameters (see Equation (20)).

NGC 4736 constitutes another interesting example. At radii larger than 225″ (~6 kpc), a pronounced anti-truncation can be clearly seen in its light profiles at all wavelengths. The bulge dominates the emission at $r \lesssim 75''$ (~2 kpc), and a prominent star-forming ring is visible at $r \simeq 40''$(~1 kpc). Both the outer disk and the bulge (together with the ring) were excluded when performing the fit, and the best-fitting model is very successful at reproducing the multi-band profiles of the inner disk, but again overestimates the true FUV and NUV profiles. Trujillo et al. (2009) carried out a detailed analysis of this galaxy by fitting its spectral energy distribution (SED) at different radii, and also by performing smoothed particle hydrodynamics simulations. These authors favor a scenario where an oval distortion gives rise to both the outer disk and the enhanced central star formation activity, involving radial flows which of course the BP00 models do not consider.

Even though the particular objects described above are rather extreme, Figure 18 shows that the model is still quite off in the UV for many objects with seemingly normal H I contents, including early-type spirals like NGC 3031 or NGC 2841 (see Figure 3). In these cases, any external interaction probably plays a minor role compared to the larger failings of the models for predicting gas contents. As mentioned at the end of Section 2.2, the BP00 models parameterize the gas infall rate as a function of both the local mass surface density and the total mass of the galaxy, so that infall will proceed faster in the densest parts of disks and, in general, in the most massive galaxies. Boissier (2000) showed that tuning the mass dependence of the infall rate can modify the present-day colors of galaxies. Redder stellar populations can be obtained if gas infall in massive early-type disks takes place even faster and earlier than in the finally adopted version of the model. Further investigation in this direction is left for future papers.

6.3. Implications for the Inside-out Growth of Disks

After having analyzed the strengths and weaknesses of the BP00 models, here we discuss the implications of the model fitting results regarding the inside-out growth of spiral disks. First, we will compare the predicted and observed color profiles in our sample, to ascertain which aspects of disk evolution can be reproduced by the models and which ones would require

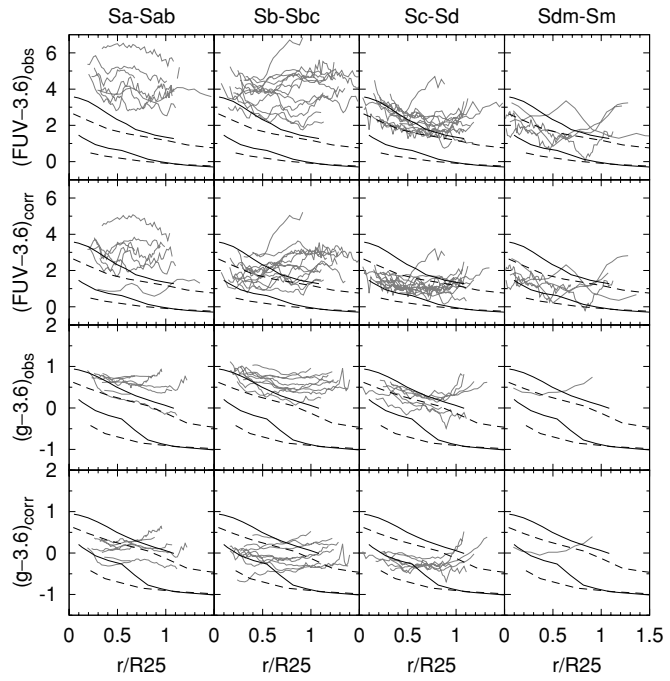

Figure 19. Comparison between the model and observed (FUV − 3.6 μm) and (g − 3.6 μm) color profiles (only those galaxies with SDSS data appear in the bottom panels). Gray lines show the color profiles of our galaxies, both before and after correcting for internal extinction ("obs" and "corr," respectively). The black lines correspond to model color profiles (with the K01 IMF) for values of λ and V_C that roughly encompass most values found in our sample. Solid lines have $\lambda = 0.03$, and dashed ones have $\lambda = 0.09$. Within each pair of profiles, the upper and redder one corresponds to $V_C = 360$ km s^{-1}, while the lower and bluer one has $V_C = 80$ km s^{-1}.

a more complex approach (such as N-body simulations). With these limitations in mind, we will then study the size evolution of our disks since $z = 1$ assuming that, at least to first order, they have evolved as dictated by the model that best fits their current multi-wavelength profiles.

6.3.1. Color Profiles

In Figure 19, we compare the color profiles of our galaxies with those predicted by the model. The gray lines show the color profiles within the radial range used in the fitting (that is, excluding the bulges). The black lines show the model predictions (using the K01 IMF) for selected values of λ and V_C that roughly bracket the values found for most of our galaxies. The solid lines correspond to $\lambda = 0.03$, and the dashed ones to $\lambda = 0.09$. Within each pair of lines, the upper (that is, redder) one has $V_C = 360$ km s^{-1}, whereas the lower one has $V_C = 80$ km s^{-1}. Two sets of color profiles are shown: (FUV − 3.6 μm) profiles and (g − 3.6 μm) ones, both of them with and without correcting for internal extinction.

Even after accounting for the effect of dust attenuation, the (FUV − 3.6 μm) profiles of Sa–Sbc galaxies fall outside the region of the diagram delineated by the model predictions. This is a direct consequence of the failure of the models at reproducing the UV profiles in early-type disks, as extensively discussed in the previous sections. In later types, however, the agreement is excellent once extinction is taken into account (the difference is minimal in Sdm–Sm galaxies, since they are not particularly dusty).

The discrepancies become much less severe redward of the Balmer break. After correcting for internal extinction, the model predictions for the (g − 3.6 μm) profiles nicely encompass the actual color profiles of our galaxies from early to late Hubble types. As we already showed in Figure 3 with NGC 2841, the models are capable of reproducing the optical and near-IR profiles of early-type disks even when they fail in the UV.

However, the color profiles of our galaxies become redder at large galactocentric distances, thus exhibiting a U-like shape. Note that the fact that we can acceptably fit the light profiles but not the color ones is not necessarily contradictory. Our models can reproduce the globally exponential nature of disks, but are not sensible to small variations such as those that can lead to the observed color profiles.

These U-shaped profiles appear to be common both in nearby (Bakos et al. 2008) and distant galaxies (Azzollini et al. 2008a). N-body simulations show that they may result from a combination of a drop in the SFR (seeded by warps in the gaseous disk, radial distribution of angular momentum, misalignment between the rotation of the infalling gas and the disk, etc.) and radial stellar migration, which would populate the outskirts of disk with old stars formed inward (Roškar et al. 2008; Martínez-Serrano et al. 2009; Sánchez-Blázquez et al. 2009). Unfortunately, none of these processes can be easily translated into an analytic one-dimensional scheme such as ours without introducing too many unconstrained free variables.

However, the simplicity of our models—compared to N-body simulations—comes at the advantage of being able to easily generate large grids of models over a wide range of halo masses and spins. Until similar grids of N-body disk simulations become available, the BP00 constitute a reasonable first-order approach to infer a galaxy's past evolution from its present-day photometric profiles.

6.3.2. A First Look at the Past Evolution of SINGS Disks

We have already checked that the model is able to reproduce the observed circular velocities of our galaxies, as well as the expected values of the spin parameter—both of which seem to be unaffected by our particular choice of IMF. In addition, we have also carefully explored some physical reasons that may be responsible for the failure of the model at reproducing the UV profiles of some early-type disks, which may hamper the study of the recent SFH in these objects. We can now proceed to study the evolution of the objects in our sample, by assuming that, at least on timescales of a few Gyr, our disks have evolved in a similar way as the corresponding model that best fits its present-day multi-wavelength profiles (see also Boissier & Prantzos 2001 for a detailed analysis of the evolution with redshift of several physical properties of galaxies).

For each model characterized with a particular pair of values of λ and V_C, we determine the disk scale length R_d at each epoch t by fitting an exponential law to the total stellar mass density profile:

$$\Sigma_{\rm stars}(r, t) = \Sigma_{\rm stars}(0, t)e^{-r/R_d(t)}. \quad (21)$$

In Figure 20, we show the temporal evolution of the disk scale length for selected values of λ and V_C. As expected, R_d increases with time in all cases. At any given epoch, the most extended disks are those with larger values of either parameter, as we already pointed out in Figure 1.

The curves describing the growth rate of R_d seem to get steeper with increasing V_C at fixed λ. In order to quantify the slope of these curves, we have performed a linear fit to R_d as a

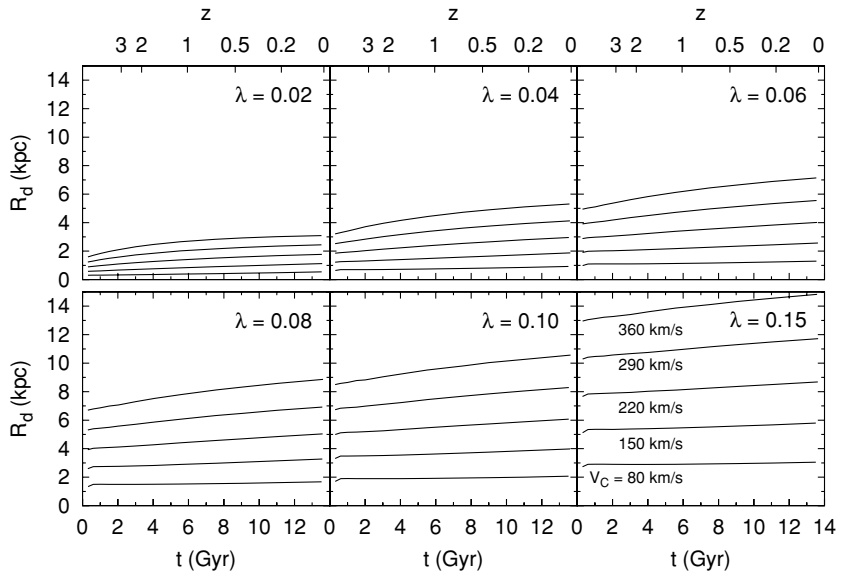

Figure 20. Temporal evolution of the exponential scale length R_d of the total stellar mass density profiles. For each value of the spin parameter λ we have plotted the curves corresponding to five selected circular velocities, as labeled in the bottom right panel.

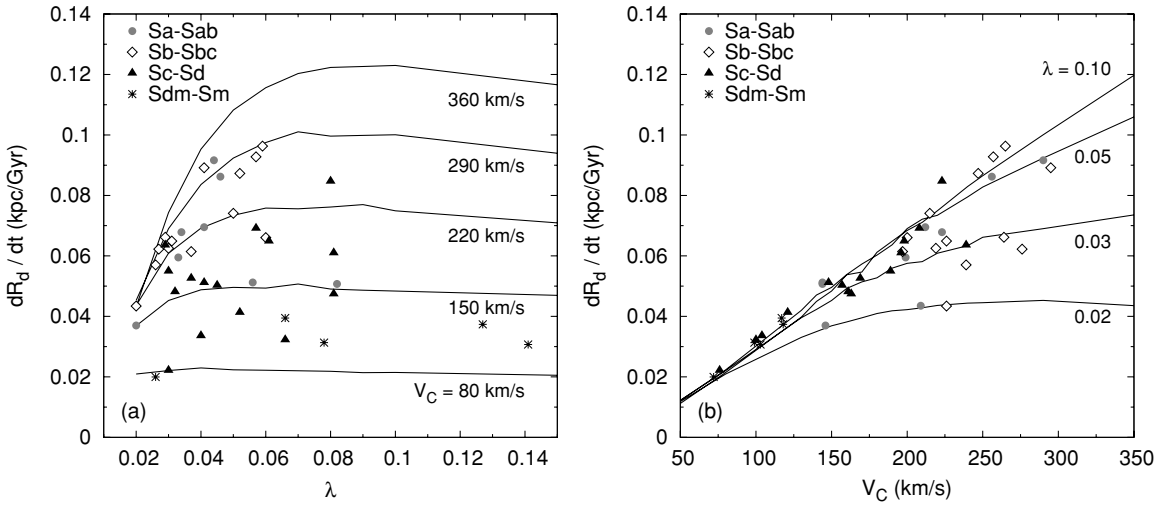

Figure 21. Growth rate of the scale length of the stellar mass density profiles, as a function of (a) λ and (b) V_C. The growth rate has been computed by fitting R_d as a function of t between $z = 1$ and $z = 0$. Observed morphological types are coded with different symbols.

function of time between $z = 1$ and $z = 0$. Disk growth seems to be approximately linear since $z = 1$ and, as mentioned in the previous sections, it is not clear whether the models can describe disk evolution beyond that redshift, when mergers were more frequent and the thin disk was not fully assembled.

In Figure 21, we plot the disk growth rate dR_d/dt as a function of both the spin parameter and the rotational velocity. The growth rate increases up to $\lambda \sim 0.06$, but for larger values it seems to be largely insensitive to the particular spin of the galaxy. It is clear that dR_d/dt mainly depends on the circular velocity, while the spin parameter only seems to be relevant at large velocities. In general, very late type disks appear to grow at a rate of 0.02–0.04 kpc Gyr^{-1}; early-type spirals, on the other hand, can increase their scale lengths at a rate up to ∼0.1 kpc Gyr^{-1}, depending on their spin.

Rather than describing the evolution of disks in terms of their *absolute* growth rate in kpc Gyr^{-1}, it is perhaps more illustrative to focus on their *relative* size increase. We have plotted in Figure 22 the ratio of the scale length of the stellar mass profiles at $z = 0$ relative to $z = 1$. Interestingly, this size ratio is essentially a unique function of the spin, with almost no dependence on V_C—and hence on mass. It might seem striking that high-spin galaxies experience almost no change in size since $z = 1$. However, as Figure 20 demonstrates, these galaxies will already exhibit extended stellar mass profiles at $z = 1$. Therefore, even if the absolute growth rate is high, it will not have a significant impact on the relative increment in size.

Can we extrapolate the conclusions obtained for our sample to the general population of disk-like galaxies? The histograms in Figure 23 show the distribution of both the absolute and relative growth rates in our sample. Both distributions peak around the values typical for galaxies similar to the MW, with an absolute growth rate of about 0.05–0.06 kpc Gyr^{-1} and a relative size increase roughly equal to 20%–25% since $z = 1$.

We should not blindly extend these results to the entire population of spiral galaxies in the Local Universe. The absolute growth rate depends primarily on V_C and, as we discussed in Section 6.1.1, low-mass disks are considerably

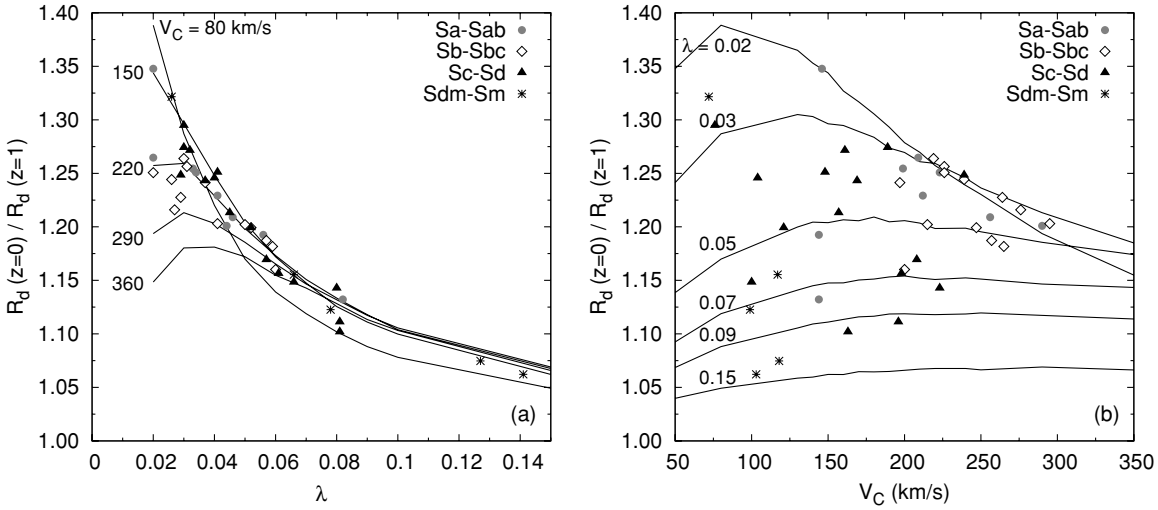

Figure 22. Ratio of the stellar disk scale lengths at $z = 0$ and $z = 1$ as a function of the (a) spin and (b) the rotational velocity. Observed morphological types are coded with different symbols.

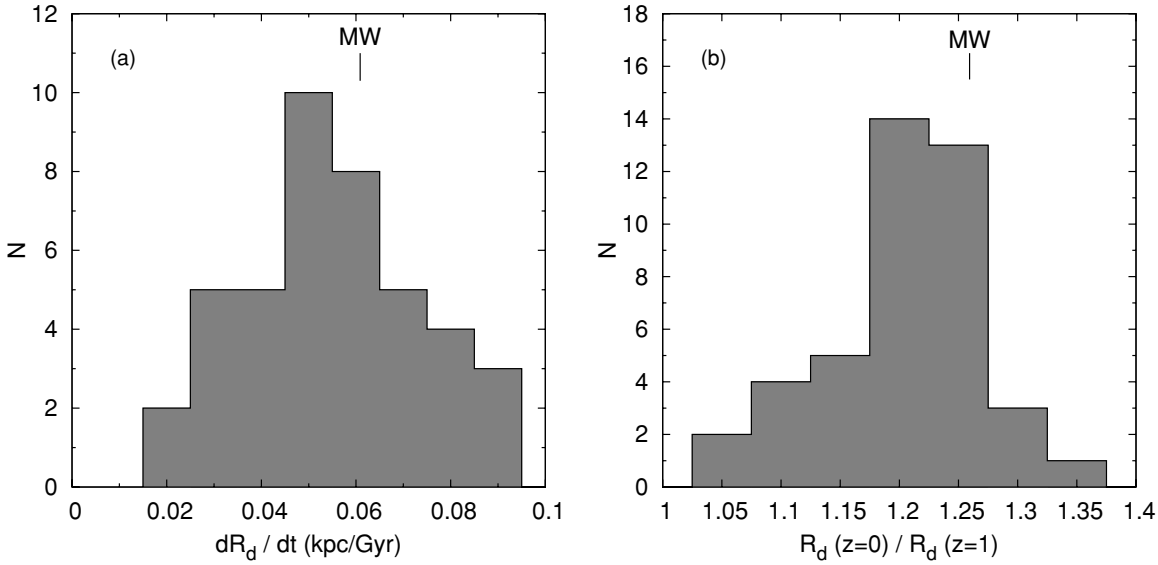

Figure 23. Distribution of the (a) absolute growth rate and (b) relative size increase in our sample. The values for an MW-like galaxy, with $\lambda = 0.03$ and $V_C = 220$ km s^{-1}, have been marked as a reference.

underrepresented in our sample. Therefore, most disks in a volume-limited sample would likely grow at slower rates than the peak value in Figure 23.

However, the situation is different regarding the relative increment in size. As we stated in Section 6.1.1, the distribution of spin values in our sample matches reasonably well the one found in *N*-body simulations of disk formation. Therefore, we can treat our sample as being representative of a complete one regarding any λ-dependent quantity. This is precisely the case with the relative size ratio, which depends almost entirely on λ alone according to Figure 22. Therefore, we can safely conclude that most disks have probably undergone an increase of 20%–25% in their scale lengths since $z = 1$ until now, regardless of their total mass. This result is in perfect agreement with the growth rate we estimated in Muñoz-Mateos et al. (2007) on a larger sample of galaxies, but using only extinction-corrected FUV and K_S-band profiles plus a very simple toy model of disk growth.

It is interesting to compare our theoretical expectations for inside-out disk growth with actual measurements of disk sizes at different redshifts. From an observational perspective, this issue is typically addressed by studying the evolution (or lack thereof) in the magnitude–size and mass–size relations, the average surface brightness and the size number density (Schade et al. 1996; Lilly et al. 1998; Simard et al. 1999; Ravindranath et al. 2004; Trujillo et al. 2004, 2006; Barden et al. 2005; McIntosh et al. 2005; Trujillo & Pohlen 2005; Azzollini et al. 2008b). The results of such studies are sometimes contradictory, due to selection effects and the inherent difficulty in disentangling the evolution of individual galaxies from the evolution of a population of galaxies as a whole.

Boissier & Prantzos (2001) confronted their predicted size–luminosity trend with several observed data sets from the literature. Here we revisit this issue and compare our model with the mass–size relation derived by Barden et al. (2005). These authors determined disk effective radii at various z by fitting a Sérsic model (Sérsic 1968) to *Hubble Space Telescope* images from GEMS (Galaxy Evolution from Morphologies and SEDs; Rix et al. 2004). Stellar masses were derived from SED

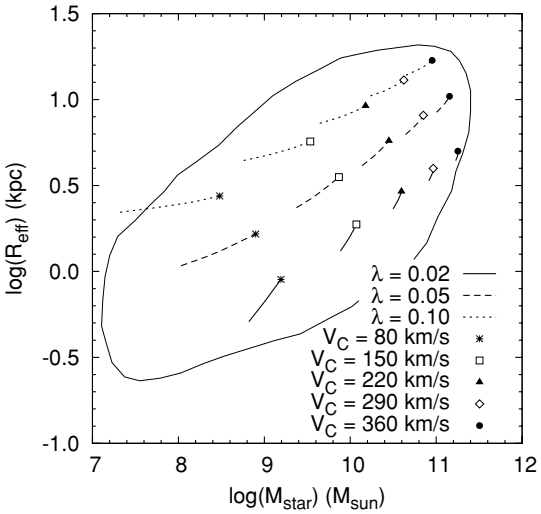

Figure 24. Evolution of the effective radius and total stellar mass of our model galaxies. The effective radius was obtained by fitting a Sérsic model to the stellar mass profiles at different z. Each track follows the evolution of a model disk from $z = 1$ to $z = 0$ (the $z = 0$ step is marked with a symbol). The corresponding spins and circular velocities of each model are indicated with different line styles and symbols, respectively. The closed curve shows the observed mass–size relation from Barden et al. (2005).

fitting to COMBO-17 data for the same objects. As a local anchor for their study they relied on a sample of nearby galaxies from SDSS. These authors found little or no evolution with z in the mass–size relation. Assuming that galaxies can only become more massive with time, they argued that they should also increase their sizes accordingly.

To replicate these measurements, for each one of our model disks we fitted a Sérsic profile to the radial distribution of stellar masses at different epochs. The results are shown in Figure 24. Each track follows the evolution of the effective radius and total stellar mass of a model galaxy from $z = 1$ to $z = 0$ (the $z = 0$ step is marked with a symbol). Models with different velocities and spins are coded with different symbols and line styles, respectively. The irregular closed line encompasses the empirical data points of Barden et al. (2005), including different redshift bins between $z = 0$ and $z = 1$ (see their Figure 10).

Our model is in perfect agreement with the observed mass–size trend. Note that the effective radii in Barden et al. (2005) were corrected to the rest-frame V band, without any further correction to get the actual stellar size. Sérsic fits to our model profiles indicate that the V-band effective radii are typically 0.05–0.15 dex larger than the stellar ones, so the closed curve in Figure 24 should be shifted downward by that amount. The agreement would be still excellent; it would actually improve if we note that most galaxies are expected to lie between the $\lambda = 0.02$ and $\lambda = 0.05$ tracks, according to the λ probability distribution shown in Figure 4.

7. CONCLUSIONS

In this paper, we have fitted the UV, optical, and near-IR profiles of 42 disk-like galaxies of the SINGS sample with the models of Boissier & Prantzos (1999, 2000). In order to recover the unattenuated starlight profiles at each wavelength, we have used the radially varying TIR/UV ratio as tracer of the internal extinction. The disk evolution models are calibrated on the MW (BP99) and further extended to other disk-like galaxies through scaling laws derived from the ΛCDM scenario (BP00). By considering the gas infall in a consistent framework, the star formation activity and the subsequent chemical evolution, the models are capable of predicting the current multi-band profiles of spirals as a function of only two parameters: the maximum circular velocity of the rotation curve, V_C, and the dimensionless spin parameter, λ. By fitting the profiles of the SINGS galaxies with those predicted by the models, we have not only checked the accuracy of the models themselves, but have also used them to infer the size evolution of the SINGS galaxies. The main conclusions of this work can be summarized as follows.

1. The rotational velocities are in good agreement with those measured from observed H I rotation curves, as well as with those estimated from the TF relation. In the latter case, the values of V_C derived from the model fitting tend to be 10%–20% larger than those predicted by the TF relation, but mainly for the most massive disks.
2. Most galaxies in our sample exhibit spin values of $\lambda \sim 0.03$. In fact, even though the sample is not volume limited, its statistical distribution of spin values closely resembles the narrow distributions usually found in N-body simulations, which typically have an almost universal peak at $\lambda \sim 0.03$–0.04.
3. There is a clear, well-known trend between V_C and Hubble type, in the sense that early-type disks have larger circular velocities—and are hence more massive—than late-type ones. There is not, however, any evident trend between the morphological type and λ, which supports the findings of numerical simulations that most halos possess the same spin, regardless of their total mass or mass assembly history.
4. While there is excellent agreement between the model predictions and the observed profiles in the optical and near-IR bands, significant departures may arise in the UV bands, depending on the morphological type and the particular choice of IMF. The Kroupa (2001) IMF yields excellent results in Sc–Sd spirals, but overestimates the UV luminosity in early-type disks, and to a much lesser extent in Sdm–Sm ones. The Kroupa et al. (1993) IMF brings the UV model profiles into better agreement with the observed ones in Sb–Sbc spirals, as well as in Sdm–Sm ones, but at the expense of losing the excellent fits for the Sc–Sd disks. While differences in the high-mass end of the IMF might indeed play a role in very late type galaxies, it is doubtful that the IMF is behind the discrepancies in the UV predictions for early-type disks. Anyway, the values of λ and V_C are largely unaffected by the specific IMF chosen. For the H I-deficient galaxies in our sample, gas removal due to interactions with the intracluster medium is the most likely culprit. For those galaxies with normal H I masses it may be necessary to revisit the mass dependence of the gas infall rate, since the model seems to retain too much gas in these objects.
5. The metallicity gradients predicted by the models are $\sim$0.015 dex kpc^{-1} steeper than the observed ones. The central oxygen abundances depend on the IMF: the values yielded by the K93 IMF are in perfect agreement with the observed central metallicities, but those obtained with the K01 one overestimate the real values by $\sim$0.7 dex.
6. According to the models, the absolute growth rate (in kpc Gyr^{-1}) of the exponential scale length of disks depends mainly on V_C, with rapidly rotating disks expanding faster. In our sample, most galaxies have their scale lengths increased by about 0.05–0.06 kpc each Gyr. Still, this is not representative of the overall population of disks, since low-mass ones are underrepresented in our sample.

7. The ratio between the current disk scale length and that at $z = 1$ is a decreasing function of λ, with little dependence on V_C. Even though high-spin disks grow faster in absolute terms, such a rapid radial expansion does not significantly increase their scale lengths, which are already considerably large at $z = 1$. On average, most disks in our sample are now 20%–25% larger than at $z = 1$. This value can be treated as being representative of a volume-limited sample, given that our galaxies have the λ distribution expected for such a kind of sample.
8. The model predicts that disk galaxies should simultaneously increase their sizes and stellar masses as time goes by. The results of the model for a grid of values of λ and V_C provide a perfect match to the observed constancy of the mass–size relation between $z = 0$ and $z = 1$.

J.C.M.M. acknowledges the receipt of a Formación del Profesorado Universitario fellowship from the Spanish Ministerio de Educación y Ciencia, as well as finantial support from NASA JPL/Spitzer grant RSA 1374189 provided for the S^{4}G project. A.G.dP. is also financed by the Spanish Ramón y Cajal program. J.C.M.M., A.G.dP., J.Z., and J.G. are partially financed by the Spanish Programa Nacional de Astronomía y Astrofísica under grants AYA2006-02358 and AyA2009-10368. They are also partly supported by the Consolider-GTC program under grant CSD2006-00070 and the AstroMadrid project (CAM S2009/ESP-1496). Part of this work was performed during a three-month stay at the Laboratoire d'Astrophysique de Marseille (LAM). J.C.M.M. thanks the Spanish Ministerio de Educación y Ciencia for providing the necessary funds, as well as the LAM staff for their support and warm hospitality. He also acknowledges support from the National Radio Astronomy Observatory, which is a facility of the National Science Foundation operated under cooperative agreement by Associated Universities, Inc. We also thank THINGS members A. Leroy and F. Walter for kindly providing the H I radial profiles in advance of publication. We also thank the anonymous referee for providing valuable comments that have improved the paper.

GALEX (*Galaxy Evolution Explorer*) is a NASA Small Explorer, launched in 2003 April. We gratefully acknowledge NASA's support for construction, operation, and science analysis for the *GALEX* mission, developed in cooperation with the Centre National d'Études Spatiales of France and the Korean Ministry of Science and Technology. This work is part of SINGS, the *Spitzer* Infrared Nearby Galaxies Survey. The *Spitzer Space Telescope* is operated by the Jet Propulsion Laboratory, Caltech, under NASA contract 1403.

Funding for the SDSS and SDSS-II has been provided by the Alfred P. Sloan Foundation, the Participating Institutions, the National Science Foundation, the U.S. Department of Energy, the National Aeronautics and Space Administration, the Japanese Monbukagakusho, the Max Planck Society, and the Higher Education Funding Council for England. The SDSS Web site is http://www.sdss.org/.

The SDSS is managed by the Astrophysical Research Consortium for the Participating Institutions. The Participating Institutions are the American Museum of Natural History, Astrophysical Institute Potsdam, University of Basel, University of Cambridge, Case Western Reserve University, University of Chicago, Drexel University, Fermilab, the Institute for Advanced Study, the Japan Participation Group, Johns Hopkins University, the Joint Institute for Nuclear Astrophysics, the Kavli Institute for Particle Astrophysics and Cosmology, the Korean Scientist Group, the Chinese Academy of Sciences (LAMOST), Los Alamos National Laboratory, the Max-Planck-Institute for Astronomy (MPIA), the Max-Planck-Institute for Astrophysics (MPA), New Mexico State University, Ohio State University, University of Pittsburgh, University of Portsmouth, Princeton University, the United States Naval Observatory, and the University of Washington.

This publication makes use of data products from the Two Micron All Sky Survey, which is a joint project of the University of Massachusetts and the Infrared Processing and Analysis Center/California Institute of Technology, funded by the National Aeronautics and Space Administration and the National Science Foundation.

Finally, we have made use of the NASA/IPAC Extragalactic Database (NED), which is operated by the Jet Propulsion Laboratory, California Institute of Technology (Caltech) under contract with NASA.

Facilities: *GALEX*, Sloan, CTIO:1.5m, KPNO:2.1m, FLWO:2MASS, CTIO:2MASS, *Spitzer*, VLA

APPENDIX

TWO-DIMENSIONAL DISTRIBUTION OF χ^2 VALUES

When fitting multi-wavelength profiles with the disk evolution models of BP00, one must bear in mind that the circular velocity and the spin may not act as completely independent parameters. Depending on the particular shape of a galaxy's profile at different wavelengths, variations in one parameter might be compensated by variations in the other one while still providing an acceptably good fit.

In order to depict the possible internal degeneracies between λ and V_C, in this appendix we present the two-dimensional χ^2 distributions obtained for each galaxy in our sample (Figure 25). Even though we keep track of the individual χ^2 distributions corresponding to each particular band for each galaxy, the plots presented here show the distribution of total χ^2 values taking into account all bands. The best-fitting model is marked with a white dot, and the area encompassing all models with $\chi \leqslant 2\chi_{\rm min}$ has been delimited with a white closed line. The same range in λ and V_C is displayed in all panels, except for the small subset of galaxies requiring larger spins and/or lower circular velocities than those in our initial grid. For the sake of clarity, those galaxies have been grouped together at the end.

In general, some galaxies exhibit some degree of anticorrelation between both parameters for low and intermediate values of λ, since the increment in the radial scale length caused by augmenting λ can be partly compensated by decreasing V_C. In some other objects, the χ^2 distribution around the best-fitting model does not show any significant degeneracy. Finally, for large values of the spin the correlation is positive: further incrementing λ significantly decreases the central surface brightness, which can be compensated to some extent by increasing V_C—even though this tends to augment the radial scale length as well.

The fact that the spin parameter is not as strongly constrained as the circular velocity is mainly due to the different way in which both quantities affect the radial profiles (Figure 1). Modifying V_C will shift the model profiles above or below the observed ones, thus rapidly increasing the χ^2 value. Varying λ, on the other hand, will mainly change the scale length alone. Given that the observed profiles exhibit inhomogeneities that deviate from our smooth predictions, this leaves some room for varying λ while still obtaining a good fit.

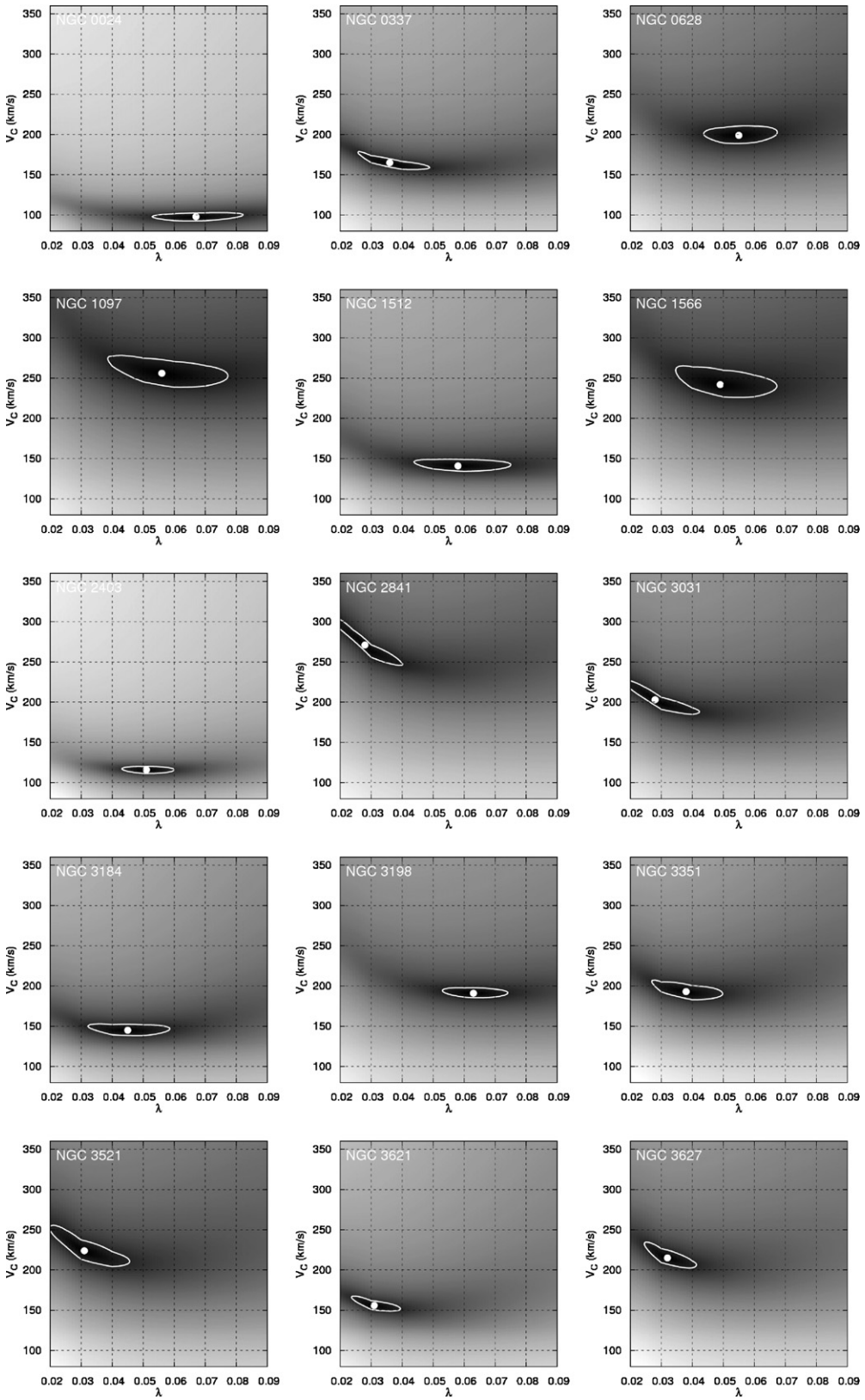

Figure 25. Two-dimensional χ^2 distributions for the galaxies in our sample. Darker shades of gray correspond to lower values of χ^2. The values of λ and V_C corresponding to the best-fitting model have been marked with a white dot. The white curved line encloses all models that satisfy $\chi^2 \leqslant 2\chi^2_{\rm min}$.

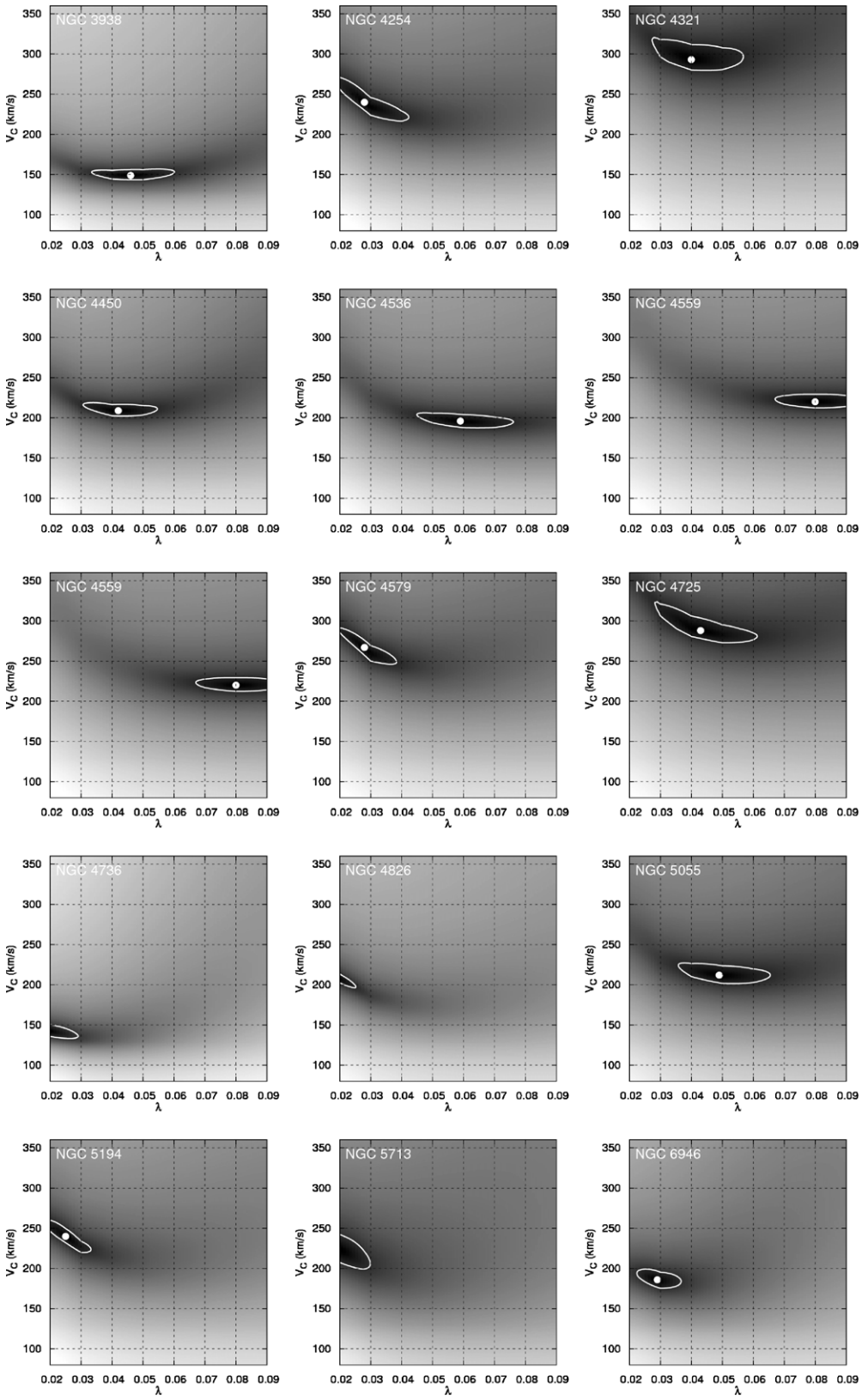

Figure 25. (Continued)

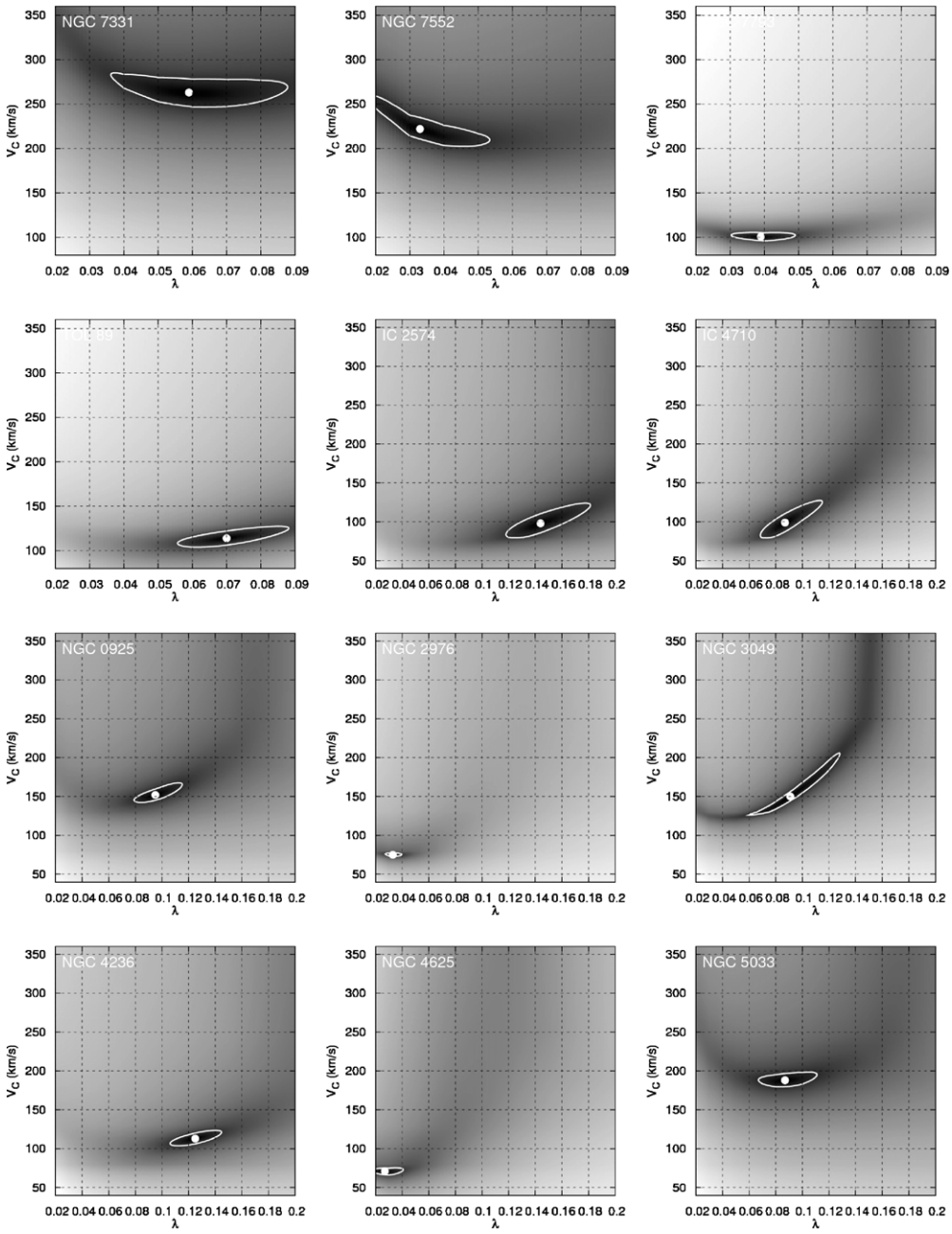

Figure 25. (Continued)

REFERENCES

Adelman-McCarthy, J. K., et al. 2008, ApJS, 175, 297
Avni, Y. 1976, ApJ, 210, 642
Azzollini, R., Trujillo, I., & Beckman, J. E. 2008a, ApJ, 679, 69
Azzollini, R., Trujillo, I., & Beckman, J. E. 2008b, ApJ, 684, 1026
Bakos, J., Trujillo, I., & Pohlen, M. 2008, ApJ, 683, 103
Barden, M., et al. 2005, ApJ, 635, 959
Barker, M. K., Ferguson, A. M. N., Cole, A. A., Ibata, R., Irwin, M., Lewis, G. F., Smecker-Hane, T. A., & Tanvir, N. R. 2011, MNRAS, 410, 504
Barnes, J., & Efstathiou, G. 1987, ApJ, 319, 575
Bastian, N., Covey, K. R., & Meyer, M. R. 2010, ARA&A, 48, 339
Bell, E. F., & de Jong, R. S. 2000, MNRAS, 312, 497
Bell, E. F., & de Jong, R. S. 2001, ApJ, 550, 212
Bell, E. F., McIntosh, D. H., Katz, N., & Weinberg, M. D. 2003, ApJS, 149, 289
Blanton, M. R., & Moustakas, J. 2009, ARA&A, 47, 159
Boissier, S. 2000, PhD thesis, Institut d'Astrophysique de Paris
Boissier, S., Boselli, A., Prantzos, N., & Gavazzi, G. 2001, MNRAS, 321, 733
Boissier, S., Buat, V., & Ilbert, O. 2010, A&A, 522, 18
Boissier, S., & Prantzos, N. 1999, MNRAS, 307, 85 (BP99)
Boissier, S., & Prantzos, N. 2000, MNRAS, 312, 398 (BP00)
Boissier, S., & Prantzos, N. 2001, MNRAS, 325, 321
Boissier, S., Prantzos, N., Boselli, A., & Gavazzi, G. 2003, MNRAS, 346, 1215
Boselli, A., Boissier, S., Cortese, L., Buat, V., Hughes, T. M., & Gavazzi, G. 2009, ApJ, 706, 1527
Boselli, A., Boissier, S., Cortese, L., Gil de Paz, A., Seibert, M., Madore, B. F., Buat, V., & Martin, D. C. 2006, ApJ, 651, 811
Boselli, A., & Gavazzi, G. 1994, A&A, 283, 12
Boselli, A., & Gavazzi, G. 2006, PASP, 118, 517
Boselli, A., & Gavazzi, G. 2009, A&A, 508, 201
Boselli, A., Gavazzi, G., & Sanvito, G. 2003, A&A, 402, 37
Boselli, A., Lequeux, J., & Gavazzi, G. 2002, A&A, 384, 33
Bosma, A. 1978, PhD thesis, Groningen Univ.
Braun, R., Walterbos, R. A. M., & Kennicutt, R. C., Jr. 1992, Nature, 360, 442
Brook, C. B., Kawata, D., Martel, H., Gibson, B. K., & Bailin, J. 2006, ApJ, 639, 126
Brooks, A., et al. 2011, ApJ, 728, 51
Buat, V., & Xu, C. 1996, A&A, 306, 61
Buat, V., et al. 2005, ApJ, 619, 51

Bullock, J. S., Dekel, A., Kolatt, T. S., Kravtsov, A. V., Klypin, A. A., Porciani, C., & Primack, J. R. 2001, ApJ, 555, 240
Carigi, L., Peimbert, M., Esteban, C., & García-Rojas, J. 2005, ApJ, 623, 213
Cervantes-Sodi, B., Hernandez, X., Park, C., & Kim, J. 2008, MNRAS, 388, 863
Chiappini, C., Matteucci, F., & Gratton, R. 1997, ApJ, 477, 765
Chiappini, C., Matteucci, F., & Romano, D. 2001, ApJ, 554, 1044
Cortese, L., Boselli, A., Franzetti, P., Decarli, R., Gavazzi, G., Boissier, S., & Buat, V. 2008, MNRAS, 386, 1157
Courteau, S., Dutton, A. A., van den Bosch, F. C., MacArthur, L. A., Dekel, A., McIntosh, D. H., & Dale, D. A. 2007, ApJ, 671, 203
Daigle, O., Carignan, C., Amram, P., Hernandez, O., Chemin, L., Balkowski, C., & Kennicutt, R. 2006, MNRAS, 367, 469
Dale, D. A., Giovanelli, R., Haynes, M. P., Scodeggio, M., Hardy, E., & Campusano, L. E. 1997, AJ, 114, 455
Dale, D. A., et al. 2007, ApJ, 655, 863
de Blok, W. J. G., Walter, F., Brinks, E., Trachternach, C., Oh, S.-H., & Kennicutt, R. C. 2008, AJ, 136, 2648
de Jong, R. S. 1996, A&A, 313, 377
de Vaucouleurs, G., de Vaucouleurs, A., Corwin, H. G., Buta, R. J., Paturel, G., & Fouqué, P. 1991, Third Reference Catalogue of Bright Galaxies (Berlin: Springer) (RC3)
Dicaire, I., et al. 2008, MNRAS, 385, 553
Draine, B. T., et al. 2007, ApJ, 663, 866
Fall, S. M., & Efstathiou, G. 1980, MNRAS, 193, 189
Fazio, G. G., et al. 2004, ApJS, 154, 10
Ferguson, A. M. N., & Clarke, C. J. 2001, MNRAS, 325, 781
Ferreras, I., & Silk, J. 2001, ApJ, 557, 165
Gardner, J. P. 2001, ApJ, 557, 616
Garnett, D. R. 2002, ApJ, 581, 1019
Garnett, D. R., Shields, G. A., Skillman, E. D., Sagan, S. P., & Dufour, R. J. 1997, ApJ, 489, 63
Gil de Paz, A., et al. 2007, ApJS, 173, 185
Gogarten, S. M., et al. 2010, ApJ, 712, 858
Gonzalez, A. H., Williams, K. A., Bullock, J. S., Kolatt, T. S., & Primack, J. R. 2000, ApJ, 528, 145
Gordon, K. D., Clayton, G. C., Misselt, K. A., Landolt, A. U., & Wolff, M. J. 2003, ApJ, 594, 279
Gordon, K. D., Clayton, G. C., Witt, A. N., & Misselt, K. A. 2000, ApJ, 533, 236
Haynes, M. P., & Giovanelli, R. 1984, AJ, 89, 758
Henry, R. B. C., & Worthey, G. 1999, PASP, 111, 919
Hernandez, X., & Cervantes-Sodi, B. 2006, MNRAS, 368, 351
Hernandez, X., Park, C., Cervantes-Sodi, B., & Choi, Y.-Y. 2007, MNRAS, 375, 163
Jarrett, T. H., Chester, T., Cutri, R., Schneider, S. E., & Huchra, J. P. 2003, AJ, 125, 525
Kennicutt, R. C., Jr. 1998, ARA&A, 36, 189
Kennicutt, R. C., Jr., et al. 2003, PASP, 115, 928
Kewley, L. J., & Ellison, S. L. 2008, ApJ, 681, 1183
Kobulnicky, H. A., & Kewley, L. J. 2004, ApJ, 617, 240
Kroupa, P. 2001, MNRAS, 322, 231 (K01)
Kroupa, P., Tout, C. A., & Gilmore, G. 1993, MNRAS, 262, 545 (K93)
Krumholz, M. R., & McKee, C. F. 2008, Nature, 451, 1082
Lee, J., et al. 2009, ApJ, 706, 599
Leroy, A. K., Walter, F., Brinks, E., Bigiel, F., de Blok, W. J. G., Madore, B. F., & Thornley, M. D. 2008, AJ, 136, 2782
Li, A., & Draine, B. T. 2001, ApJ, 554, 778
Lilly, S., et al. 1998, ApJ, 500, 75
MacArthur, L. A., Courteau, S., Bell, E., & Holtzman, J. A. 2004, ApJS, 152, 175
Martin, D., et al. 2005, ApJ, 619, 1
Martin, P., & Roy, J.-R. 1994, ApJ, 424, 599
Martínez-Serrano, F. J., Serna, A., Doménech-Moral, M., & Domínguez-Tenreiro, R. 2009, ApJ, 705, 133
Matteucci, F., & François, P. 1989, MNRAS, 239, 885
Meurer, G. R., Heckman, T. M., & Calzetti, D. 1999, ApJ, 521, 64
Meurer, G. R., et al. 2009, ApJ, 695, 765
McIntosh, D. H., et al. 2005, ApJ, 632, 191
Mo, H. J., Mao, S., & White, S. D. M. 1998, MNRAS, 295, 319
Moustakas, J., & Kennicutt, R. C., Jr. 2006, ApJ, 651, 155
Moustakas, J., Kennicutt, R. C., Jr., Tremonti, C. A., Dale, D. A., Smith, J.-D. T., & Calzetti, D. 2010, ApJS, 190, 233
Molla, M., Ferrini, F., & Diaz, A. I. 1996, ApJ, 466, 668
Muñoz-Mateos, J. C., et al. 2007, ApJ, 658, 1006
Muñoz-Mateos, J. C., et al. 2009a, ApJ, 703, 1569 (Paper I)
Muñoz-Mateos, J. C., et al. 2009b, ApJ, 701, 1965 (Paper II)
Pagel, B. E. J., Edmunds, M. G., Blackwell, D. E., Chun, M. S., & Smith, G. 1979, MNRAS, 189, 95
Paturel, G., Petit, C., Prugniel, P., Theureau, G., Rousseau, J., Brouty, M., Dubois, P., & Cambrésy, L. 2003, A&A, 412, 45
Pflamm-Altenburg, J., Weidner, C., & Kroupa, P. 2007, ApJ, 671, 1550
Pflamm-Altenburg, J., Weidner, C., & Kroupa, P. 2009, MNRAS, 395, 394
Pilyugin, L. S., & Thuan, T. X. 2005, ApJ, 631, 231
Pilyugin, L. S., Vílchez, J. M., & Contini, T. 2004, A&A, 425, 849
Pizagno, J., et al. 2007, AJ, 134, 945
Prantzos, N., & Boissier, S. 2000, MNRAS, 313, 338
Press, W. H., Teukolsky, S. A., Vetterling, W. T., & Flannery, B. P. 1992, Numerical Recipes in C. The Art of Scientific Computing (Cambridge: Cambridge Univ. Press)
Ravindranath, S., et al. 2004, ApJ, 604, 9
Rieke, G. H., et al. 2004, ApJS, 154, 25
Rix, S., et al. 2004, ApJ, 152, 163
Roberts, M. S. 1978, AJ, 83, 1026
Roškar, R., Debattista, V. P., Stinson, G. S., Quinn, T. R., Kaufmann, T., & Wadsley, J. 2008, ApJ, 675, 65
Rubin, V. C., Burstein, D., Ford, W. K., Jr., & Thonnard, N. 1985, ApJ, 289, 81
Salucci, P., & Persic, M. 1997, in ASP Conf. Ser. 117, Dark and Visible Matter in the Galaxies, ed. M. Persic & P. Salucci (San Francisco, CA: ASP), 1
Salpeter, E. E. 1955, ApJ, 121, 161
Samland, M., & Gerhard, O. E. 2003, A&A, 399, 961
Sánchez-Blázquez, P., Courty, S., Gibson, B. K., & Brook, C. B. 2009, MNRAS, 398, 591
Schade, D., Lilly, S. J., Le Fevre, O., Hammer, F., & Crampton, D. 1996, ApJ, 464, 79
Schechter, P. 1976, ApJ, 203, 297
Schlegel, D. J., Finkbeiner, D. P., & Davis, M. 1998, ApJ, 500, 525
Sellwood, J. A., & Wilkinson, A. 1993, Rep. Prog. Phys., 56, 173
Sérsic, J. L. 1968, Atlas de Galaxias Australes (Córdoba, Argentina: Observatorio Astronómico)
Shaver, P. A., McGee, R. X., Newton, L. M., Danks, A. C., & Pottasch, S. R. 1983, MNRAS, 204, 53
Simard, L., et al. 1999, ApJ, 519, 563
Smartt, S. J., & Rolleston, W. R. J. 1997, ApJ, 481, 47
Solanes, J. M., Giovanelli, R., & Haynes, M. P. 1996, ApJ, 461, 609
Solanes, J. M., Manrique, A., García-Gómez, C., González-Casado, G., Giovanelli, R., & Haynes, M. P. 2001, ApJ, 548, 97
Spergel, D. N., et al. 2007, ApJS, 170, 377
Springel, V., et al. 2005, Nature, 435, 629
Syer, D., Mao, S., & Mo, H. J. 1999, MNRAS, 305, 357
Taylor, V. A., Jansen, R. A., Windhorst, R. A., Odewahn, S. C., & Hibbard, J. E. 2005, ApJ, 630, 784
Tinsley, B. M. 1980, Fundam. Cosm. Phys., 5, 287
Trujillo, I., Martinez-Valpuesta, I., Martínez-Delgado, D., Peñarrubia, J., Gabany, R. J., & Pohlen, M. 2009, ApJ, 704, 618
Trujillo, I., & Pohlen, M. 2005, ApJ, 630, 17
Trujillo, I., et al. 2004, ApJ, 604, 521
Trujillo, I., et al. 2006, ApJ, 650, 18
Tully, R. B., & Fisher, J. R. 1977, A&A, 54, 661
van den Bergh, S. 1976, ApJ, 206, 883
van Zee, L., Salzer, J. J., Haynes, M. P., O'Donoghue, A. A., & Balonek, T. J. 1998, AJ, 116, 2805
Verheijen, M. A. W. 2001, ApJ, 563, 694
Vitvitska, M., Klypin, A. A., Kravtsov, A. V., Wechsler, R. H., Primack, J. R., & Bullock, J. S. 2002, ApJ, 581, 799
Walter, F., Brinks, E., de Blok, W. J. G., Bigiel, F., Kennicutt, R. C., Jr., Thornley, M. D., & Leroy, A. K. 2008, AJ, 136, 2563
Warren, M. S., Quinn, P. J., Salmon, J. K., & Zurek, W. H. 1992, ApJ, 399, 405
Weidner, C., & Kroupa, P. 2005, ApJ, 625, 754
Werner, M. W., et al. 2004, ApJS, 154, 1
White, S. D. M., & Frenk, C. S. 1991, ApJ, 379, 52
Witt, A. N., & Gordon, K. D. 2000, ApJ, 528, 799
Wyse, R. F. G., & Silk, J. 1989, ApJ, 339, 700
York, D., et al. 2000, AJ, 120, 1579
Yoshii, Y., & Sommer-Larsen, J. 1989, MNRAS, 236, 779
Zaritsky, D., Kennicutt, R. C., Jr., & Huchra, J. P. 1994, ApJ, 420, 87